JOURNAL OF GUIDANCE, CONTROL, AND DYNAMICS
Vol. 33, No. 2, March–April 2010

Analytic Theory for High-Inclination Orbits in the Restricted Three-Body Problem

Mohammed A. Ghazy* and Brett Newman†
Old Dominion University, Norfolk, Virginia 23529

DOI: 10.2514/1.41628

This paper explores the analytical solution properties surrounding a hypothetical orbit in an invariant plane perpendicular to the line joining the two primaries in the circular restricted three-body problem. Assuming motion can be maintained in the plane, Jacobi's integral equation can be analytically integrated, yielding a closed-form expression for the period and path of the third body expressed with elliptic integral and elliptic function theory. In this case, the third body traverses a circular path with nonuniform speed. In a strict sense, the in-plane assumption cannot be maintained naturally. However, the hypothetical orbit is shown to satisfy Jacobi's integral equation and the tangential motion equation exactly and the other two motion equations approximately in bounded-averaged and banded sense. More important, the hypothetical solution can be used as the basis for an iterative analytical solution procedure for the three-dimensional trajectory where corrections are computable in closed form. In addition, the in-plane assumption can be strictly enforced with the application of a modulated thrust acceleration which is expressible in closed form. Presented methodology is primarily concentrated on halo-class orbits.

Nomenclature

a	=	radius of circular orbit
C	=	Jacobi's constant
G	=	universal gravitational constant
J	=	Jacobi's function
m_1	=	mass of first primary
m_2	=	mass of second primary, $m_2 \leq m_1$
$\mathbf{r}$	=	position vector of third mass relative to center of mass
$\mathbf{r}_1$	=	position vector of first primary relative to center of mass
$\mathbf{r}_2$	=	position vector of second primary relative to center of mass
r_{12}	=	distance between two primaries
$\boldsymbol{\rho}_1$	=	position vector of third mass relative to first primary
$\boldsymbol{\rho}_2$	=	position vector of third mass relative to second primary
$\boldsymbol{\omega}$	=	angular velocity vector of rotating fame

I. Introduction

THE circular restricted three-body problem addresses the motion of an inertially negligible third body in the presence of two primary bodies undergoing circular orbital motion about their combined mass center. Solutions to this problem have great utility for mission design or celestial analysis near binary planet, star, or planet-star systems. The Earth–moon system is one of many relevant applications. Although an infinite set of transient and periodic orbits can be generated numerically for this problem, analytical solutions are not found in abundance. The importance of analytical solutions lies in their enhancement to physical understanding and the underlying framework for exploitation and synthesis.

Complete analytical formulation of special orbits in the circular restricted three-body problem is rare in the literature. The few results that do exist include the libration point solutions, the exact motion integral result, the bounding surfaces or curves of zero velocity, and the rectilinear oscillation solution [1,2]. A cornerstone of many of these results originates from the advantages that exist when the problem is formulated in a rotating coordinate system moving with the primaries. Five static (in the rotating system) equilibrium points in which gravitational and centripetal accelerations balance were found by Lagrange [3]. The libration solutions are actually special cases of the conic section solutions existing for the more general unrestricted three-body problem [1,2]. Jacobi was able to restructure the motion equations such that an exact analytic integral could be executed, leading to Jacobi's integral equation and Jacobi's constant [4]. Using the exact integral to provide boundaries to regions in which third body motion is permissible for a specified initial condition was first analyzed by Hill [5] and later Moulton [6]. A modern 3-D interpretation can be found in [7,8]. Existence of periodic rectilinear motion of the third body in the rotating frame along an axis perpendicular to the plane of motion of the primaries and passing through the center of mass was accomplished by MacMillan [9] and later revisited by Sitnikov [10] and Battin [2]. With the use of elliptic integrals, the period of motion corresponding to certain initial conditions is expressible in closed form.

Periodic solutions to the restricted problem hold special significance for several reasons [1]. Moulton [11] laid the analytical foundation for classification and solution of periodic orbits about the collinear libration points using linear analysis. Three main classes were discovered: 2-D horizontal orbits, one-dimensional vertical orbits, and 3-D orbits. These orbits were extended analytically by Moulton [11] and others, over many decades, to larger amplitudes. Szebehely [1] efficiently summarizes these efforts. At least three classes, having their origins tracable to Moulton's work are the in-plane or Lyapunov periodic orbits, the nearly vertical or out-of-plane dominated periodic orbits, and 3-D periodic halo orbits [12]. Farquhar and Kamel [13] used an analytical higher order technique to study these naturally occurring but unstable halo orbits. Richardson [14] used the linearized motion equations and their solution about collinear equilibrium points as a generating orbit to produce halo orbits through a successive analytical approximation technique applied to the full nonlinear equations of motion in which the origin is the collinear equilibrium point. A correction of the frequency and a restriction on the amplitudes of coordinates are found to be necessary for establishing such orbits. After 1980 this type of analytical work for the restricted problem was much less investigated.

Starting in the 1960s and continuing through the present time, numeric computation has been used to construct and investigate periodic orbits residing in the restricted three-body gravitation field.

Presented as Paper 6430 at the Astrodynamics Specialist Conference, Honolulu, HI, 18–21 Aug. 2008; received 21 Oct. 2008; accepted for publication 28 Sept. 2009.

*Doctoral Candidate, Department of Aerospace Engineering. Student Member AIAA.

†Professor, Department of Aerospace Engineering. Associate Fellow AIAA.

Construction of periodic orbits is achieved by searching for an appropriate initial condition set that, when propagated, closes on itself. Such differential correction techniques are the computational engine for many investigations [15]. Using pure computational tools, Henon showed that halo orbits result from in-plane orbit bifurcations at critical amplitudes [16]. Zagouras and Kazantzis [17], Robin and Markellos [18], and Ichtiaroglou and Michalodimitrakis [19] follow this type of approach to identify periodic families, characterize properties, and study their relationships to one another. The 1990 book by Marchal addresses more recent efforts [20]. Starting in the early 1990s, researchers began to couple dynamical systems theory with numeric computation to discover new relationships and insights pertaining to restricted three-body periodic orbits [12]. Manifold theory is central to this approach and relies heavily on computation using tangency concepts applied to the eigen structures of the monodromy matrix along a halo orbit [21], or Lindstedt-Poincaré type numeric constructions [22]. This research has shown that in-plane periodic, out-of-plane dominated periodic, 3-D periodic, and 3-D quasi-periodic orbital families constitute the 4-D center manifold for each libration point [21]. Valtonen and Karttunen [23] provide a semi-analytic approach for restricted problems based on statistical concepts, not necessarily for periodic solutions.

The objective of this research is to investigate methodology whereby approximate but pure analytical relationships between high-inclination halo type orbit characteristics and fundamental three-body system parameters can be developed [24]. Richardson [14] may be the closest work to this paper, whereas the recent computational approaches in [21,22] are only indirectly related. A major difference between this work and [14] is that a nonlinear generating orbit is used. Several advantages may exist with this generating solution. From the outset, analysis will incorporate aspects of the three-body problem that are not present in the Richardson approach until higher order terms are addressed. Next, the analysis should hold for larger radius orbits located farther from the libration points. Finally, insights afforded by analysis of the generating orbit properties are unique and not present in the Richardson work.

In this study Jacobi's integral, governing the motion of the third body in the circular restricted three-body problem, is integrated again, assuming certain characteristics for the motion of the third body even though these characteristics may be only approximately satisfied in practice. This procedure is similar to that used in the rectilinear oscillation theory [2]. Not only can an analytical formulation of the period of motion be obtained, but also a closed-form expression for the orbital path is available. Motion in two of the three axes can be solved for functionally. The projected motion on the corresponding plane is circular with nonuniform speed. The period and projected path are expressed in terms of elliptic integrals and functions. The governing characteristics do not permit motion along the third axis. An iterative procedure is used to improve the accuracy of the predicted 3-D motion. This study introduces a new approximate analytical foundation for an existing class of 3-D highly inclined quasi-periodic orbits that may be used for applications in any restricted three-body system. In Sec. II a description of the equations of motion and Jacobi's integral for the circular restricted problem of three bodies, are reviewed. In Sec. III a suppositional circular solution for the third body motion is analytically derived and the properties of the proposed orbit are discussed. In Sec. IV natural constraints imposed on the third body motion and initial condition are investigated. In Sec. V the accuracy of the supposed conditions and analytical solution are analyzed. In Sec. VI an iterative analytical procedure is offered to provide corrections to the base solution. In Sec. VII comparisons are made between a numerically propagated orbit associated with an artificial three-body system and the corresponding approximate analytical solution for the orbit. In Sec. VIII application of modulated thrust to render the original solution exactly is discussed. Finally, conclusions are drawn in Sec. IX.

II. Circular Restricted Three-Body Theory

The circular restricted three-body problem (CRTBP) [1,2] addresses the motion of a small third body when the motion of the two primary masses is restricted to the xy-plane so that they move in circular orbits relative to each other and relative to their center of mass (cm). The center of the system is located between the two primary masses on the line joining them which is aligned with the x-axis in the rotating system. The z-axis is the axis of the orbital angular velocity vector, and the y-axis is in the plane of motion of the two primaries and completes the right-hand system. The main characteristics of the circular problem are that the distance of either primary relative to the center of mass is constant, and the angular velocity of the rotating system is constant. Figure 1 shows the CRTBP geometry in the rotating coordinate system.

In Fig. 1, the xyz coordinate system with origin at the center of mass is rotating with the primaries according to angular velocity vector $\boldsymbol{\omega}$. Body masses are denoted by m_i for $i = 1, 2, 3$, where $m_3 \ll m_1$ and $m_3 \ll m_2$. Absolute position vectors to each primary are denoted by $\mathbf{r}_1$ and $\mathbf{r}_2$ (constants), whereas $\mathbf{r}$ is the corresponding vector for the third body. The relative positions of body 3 with respect to bodies 1 and 2 are denoted by $\boldsymbol{\rho}_i$, $i = 1, 2$. Components of these dimensional position vectors are

$$\begin{aligned} \mathbf{r}_i &= x_i\hat{i} \qquad , i = 1, 2 \ (x_1 > 0, x_2 < 0) \\ \mathbf{r} &= x\hat{i} + y\hat{j} + z\hat{k} \\ \boldsymbol{\rho}_i &= (x - x_i)\hat{i} + y\hat{j} + z\hat{k} \qquad , i = 1, 2 \end{aligned} \tag{1}$$

where $\hat{i}, \hat{j}, \hat{k}$ are unit vectors for the xyz-axes. Magnitudes of $\boldsymbol{\rho}_1$ and $\boldsymbol{\rho}_2$ are also given by

$$\rho_1 = [(x - x_1)^2 + y^2 + z^2]^{1/2} \qquad \rho_2 = [(x - x_2)^2 + y^2 + z^2]^{1/2} \tag{2}$$

Finally, the angular velocity vector $\boldsymbol{\omega}$ (constant) based on the circular orbit condition is

$$\boldsymbol{\omega} = \omega\hat{k} \qquad \omega^2 = \frac{G}{r_{12}^3}(m_1 + m_2) \tag{3}$$

where $r_{12} = x_1 - x_2$ and G denotes the universal gravitational constant.

The Lagrangian and Hamiltonian functions L and H for the third body in this system are

$$\begin{aligned} L &= \frac{1}{2}[(\dot{q}_1^2 + \dot{q}_2^2 + \dot{q}_3^2) + 2\omega(q_1\dot{q}_2 - q_2\dot{q}_1) + \omega^2(q_1^2 + q_2^2)] + U \\ H &= \frac{1}{2}(p_1^2 + p_2^2 + p_3^2) + \omega(p_1q_2 - p_2q_1) - U \end{aligned} \tag{4}$$

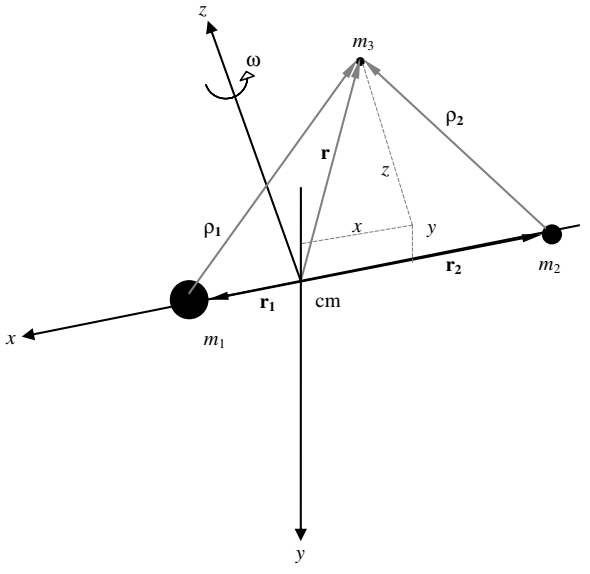

Fig. 1 Circular restricted three-body problem geometry.

where q_i for $i = 1, 2, 3$ are the generalized coordinates; p_i for $i = 1, 2, 3$ are the momenta; and U is the gravitational potential function. These quantities are defined below:

$$q_1 = x \qquad p_1 = \frac{\partial L}{\partial \dot{q}_1} \qquad q_2 = y \qquad p_2 = \frac{\partial L}{\partial \dot{q}_2} \qquad q_3 = z \qquad p_3 = \frac{\partial L}{\partial \dot{q}_3} \tag{5}$$

$$U = \frac{Gm_1}{\rho_1} + \frac{Gm_2}{\rho_2} \tag{6}$$

Using Hamilton's canonical equations

$$\begin{aligned} \frac{\mathrm{d}q_1}{\mathrm{d}t} &= p_1 + \omega q_2 & \frac{\mathrm{d}p_1}{\mathrm{d}t} &= \omega p_2 + \frac{\partial U}{\partial q_1} \\ \frac{\mathrm{d}q_2}{\mathrm{d}t} &= p_2 - \omega q_1 & \frac{\mathrm{d}p_2}{\mathrm{d}t} &= -\omega p_1 + \frac{\partial U}{\partial q_2} \\ \frac{\mathrm{d}q_3}{\mathrm{d}t} &= p_3 & \frac{\mathrm{d}p_3}{\mathrm{d}t} &= \frac{\partial U}{\partial q_3} \end{aligned} \tag{7}$$

the third body equations of motion are

$$\ddot{x} - 2\omega\dot{y} = \omega^2 x + \frac{\partial U}{\partial x} \qquad \ddot{y} + 2\omega\dot{x} = \omega^2 y + \frac{\partial U}{\partial y} \qquad \ddot{z} = \frac{\partial U}{\partial z} \tag{8}$$

To simplify the equations of motion, Jacobi's function J is introduced and defined as

$$J = \frac{1}{2}\omega^2(x^2 + y^2) + \frac{Gm_1}{\rho_1} + \frac{Gm_2}{\rho_2} \tag{9}$$

The final form of the equations of motion of the third body in the rotating system is

$$\ddot{x} - 2\omega\dot{y} = \frac{\partial J}{\partial x} \qquad \ddot{y} + 2\omega\dot{x} = \frac{\partial J}{\partial y} \qquad \ddot{z} = \frac{\partial J}{\partial z} \tag{10}$$

The dynamics of the CRTBP represented by the mathematical structure in Eq. (10) admit an exact integral. The resulting equation and constant are known as Jacobi's integral equation and the Jacobi constant C:

$$C = 2J - v^2 \tag{11}$$

In Eq. (11), v denotes the third body velocity magnitude with respect to the xyz system:

$$v^2 = \dot{x}^2 + \dot{y}^2 + \dot{z}^2 \tag{12}$$

III. Suppositional Circular Motion: $y'z'$ Plane

Figure 2 illustrates a suppositional circular motion path for the third body in the $y'z'$-plane, which is offset from the yz-plane by the constant distance d_x. This motion is not strictly permitted by the governing motion equations. However, the motion solves Jacobi's integral equation exactly, solves the tangential equation of motion exactly, and approximately solves the radial and cylindrical motion equations in bounded averaged and banded sense. The analysis for Jacobi's integral equation is contained in this section whereas the equations of motion analysis is given in Sec. V. Further, a methodology to correct this supposition with an iterative procedure will be addressed in Sec. VI.

Under the supposition, coordinates of the third body are equal to

$$x(t) = d_x \qquad y(t) = a\sin\{\theta(t)\} \qquad z(t) = a\cos\{\theta(t)\} \tag{13}$$

where a denotes the constant radius of the circular path and angle $\theta(t)$ measured from the z'-axis parameterizes the location along the path as an undetermined function of time, not necessarily linear. From the geometry in Fig. 2, or substituting Eq. (13) into Eq. (2), this path

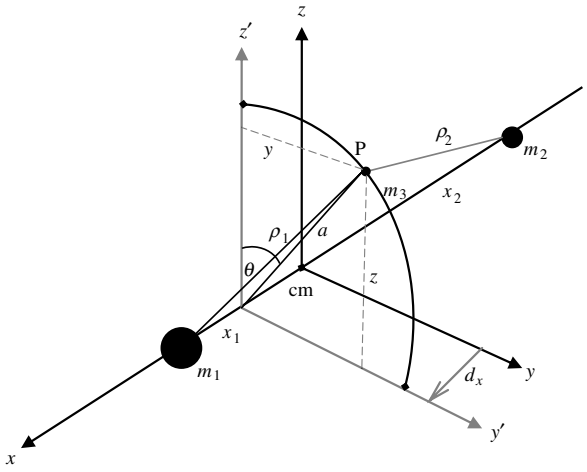

Fig. 2 Third body circular motion in $y'z'$-plane (supposition).

maintains constant separation between the two primaries and the third body:

$$\rho_1 = [(d_x - x_1)^2 + a^2]^{1/2} \qquad \rho_2 = [(d_x - x_2)^2 + a^2]^{1/2} \tag{14}$$

In Fig. 2 point P represents the location of the third body on the supposed orbit. Assuming point P_0 is the initial position of the third body, the six initial conditions are

$$\begin{aligned} &[x_0, y_0, z_0, \dot{x}_0, \dot{y}_0, \dot{z}_0] \\ &\quad = [d_x, a\sin\{\theta_0\}, a\cos\{\theta_0\}, 0, a\dot{\theta}_0\cos\{\theta_0\}, -a\dot{\theta}_0\sin\{\theta_0\}] \\ &\quad \text{at } t = t_0 \end{aligned} \tag{15}$$

where $\theta(t_0) = \theta_0$ and $\dot{\theta}(t_0) = \dot{\theta}_0$ denote the initial angular position and angular velocity of the third body. Equation (15) indicates the two independent constants θ_0 and $\dot{\theta}_0$ are all that is needed to describe the initial state of the $y'z'$ plane circular motion, assuming the radius and plane location a and d_x are specified.

Along this circular path, the rate at which $\theta(t)$ changes with time is not constant. Although the assumed orbital path for the third body is a circle, the speed at which the body travels along that path is nonuniform or accelerated. To determine the governing differential relation for the angular position, substitute the time derivatives of $x(t)$, $y(t)$, $z(t)$ into Jacobi's integral result in Eq. (11):

$$\dot{\theta}^2(t) = \omega^2\sin^2\{\theta(t)\} + \frac{1}{a^2}\left\{\omega^2 d_x^2 + 2G\left(\frac{m_1}{\rho_1} + \frac{m_2}{\rho_2}\right) - C\right\} \tag{16}$$

Note in Eq. (16) the second term in the right-hand side is a constant that is renamed C_0:

$$C_0 = \frac{1}{a^2}\left\{\omega^2 d_x^2 + 2G\left(\frac{m_1}{\rho_1} + \frac{m_2}{\rho_2}\right) - C\right\} \tag{17}$$

Constant C_0 is determinable from the initial conditions θ_0 and $\dot{\theta}_0$ existing at P_0:

$$C_0 = \dot{\theta}_0^2 - \omega^2\sin^2\{\theta_0\} \tag{18}$$

Equation (16) thus becomes

$$\dot{\theta}^2(t) = \omega^2[\sin^2\{\theta(t)\} - \sin^2\{\theta_0\}] + \dot{\theta}_0^2 \tag{19}$$

Now, an analytical solution for the period of the circular path is sought from Eq. (19). Define a new angle $\phi(t)$ for transformation purposes:

$$\phi(t) = \frac{\pi}{2} - \theta(t) \tag{20}$$

Modify Eq. (19), using the transformation variable $\phi(t)$, to a standard Legendre elliptic differential form of the first kind [25]:

$$-\frac{\mathrm{d}\phi(t)}{\mathrm{d}t} = \frac{\omega}{k}[1 - k^2\sin^2\{\phi(t)\}]^{1/2} \tag{21}$$

where k is the modulus of the elliptic form:

$$k = \left(\cos^2\{\theta_0\} + \frac{\dot{\theta}_0^2}{\omega^2}\right)^{-1/2} \tag{22}$$

A complete elliptic integral of Eq. (21) can be formed to obtain the analytical expression for the period T of the circular path. Integrating Eq. (21) over a general half path (t: $t_0 \to t_0 + T/2$, $\theta(t)$: $\theta_0 \to \theta_0 + \pi$), or

$$\int_{t_0}^{t_0+T/2} dt = -\frac{k}{\omega}\int_{\frac{\pi}{2}-\theta_0}^{-\frac{\pi}{2}-\theta_0} \frac{d\phi}{[1 + k^2\sin^2\{\phi\}]^{1/2}} \tag{23}$$

yields the period T:

$$T = \frac{4k}{\omega}K(k) \tag{24}$$

In Eq. (24), $K(k)$ is the complete elliptic integral of the first kind [25].

For the suppositional circular motion, the period is a nonlinear function of θ_0, $\dot{\theta}_0$, and ω and is independent of a and d_x. Nonlinear dependence on initial angular position and velocity is due to trigonometric, power, multiplication, and complete elliptic integral operations. Figure 3 shows the nondimensional periodicity for various nondimensional initial conditions. As expected, orbital period T and initial angular velocity $\dot{\theta}_0$ are inversely proportional. Also note, for the same initial rate larger initial positions can amplify the period. The low end cut off points for $\dot{\theta}_0$ in Fig. 3 are from dynamical constraints discussed in Sec. IV.

Next, an analytical solution for the parameterization of the circular path is sought from Eq. (19). Returning to Eq. (21), perform an integral over a general path segment (t: $t_0 \to t$, $\theta(t)$: $\theta_0 \to \theta$):

$$\int_{t_0}^{t} dt = -\frac{k}{\omega}\int_{\frac{\pi}{2}-\theta_0}^{\phi} \frac{d\phi}{[1 - k^2\sin^2\{\phi\}]^{-1/2}} \tag{25}$$

$$\frac{\omega}{k}(t - t_0) = -F(\phi(t), k) + F\left(\frac{\pi}{2} - \theta_0, k\right) \tag{26}$$

In Eq. (26), function $F(\psi, k)$ is the incomplete elliptic integral of the first kind evaluated at ψ. By using the theory of theta functions [25], Eq. (26) is inverted to obtain the transform angle $\phi(t)$ as a function of time:

$$\sin\{\phi(t)\} = \mathrm{sn}\left(-\frac{\omega}{k}(t - t_0) + F\left(\frac{\pi}{2} - \theta_0, k\right), k\right) \tag{27}$$

where $\mathrm{sn}(\tau, k)$ denotes the elliptic sine or s-n function evaluated at τ [25], precisely the inverse of $F(\phi(\tau), k)$. After transforming back to the original coordinate, analytical expressions for the parameterizing variable $\theta(t)$ for the circular path and its derivative are

$$\begin{aligned}\cos\{\theta(t)\} &= \mathrm{sn}\left(-\frac{\omega}{k}(t - t_0) + F\left(\frac{\pi}{2} - \theta_0, k\right), k\right)\\ \sin\{\theta(t)\} &= \mathrm{cn}\left(-\frac{\omega}{k}(t - t_0) + F\left(\frac{\pi}{2} - \theta_0, k\right), k\right)\end{aligned} \tag{28}$$

$$\dot{\theta}(t) = \frac{\omega}{k}\mathrm{dn}\left(-\frac{\omega}{k}(t - t_0) + F\left(\frac{\pi}{2} - \theta_0, k\right), k\right) \tag{29}$$

In Eqs. (28) and (29), $\mathrm{cn}(\tau, k)$ and $\mathrm{dn}(\tau, k)$ are the elliptic c-n and d-n functions evaluated at τ [25].

In effect, Eqs. (26–29) represent a closed form integral of Jacobi's integral equation under the imposed suppositional conditions. These results can be referred to as an "integral of the suppositional motion." Figures 4–6 show various orbital trajectory characteristics of the suppositional motion, derived from the generally applicable Eqs. (28) and (29), across a family of modulus values for the Earth–moon system (specified m_1, m_2, r_{12}), chosen only to portray graphical information for a commonly analyzed three-body system.

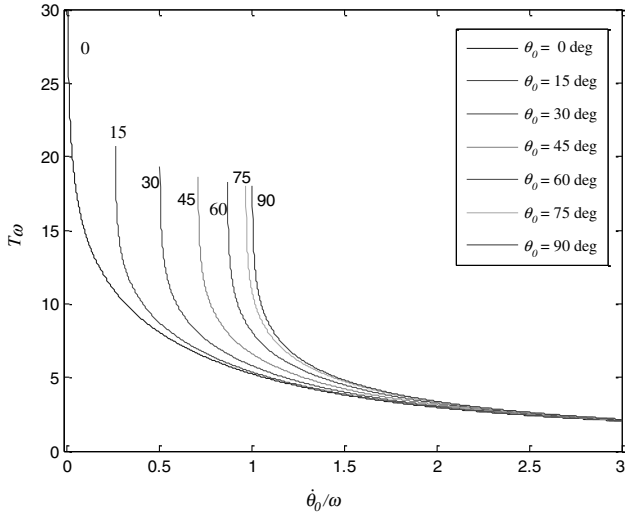

Fig. 3 Periodicity behavior of suppositional circular motion.

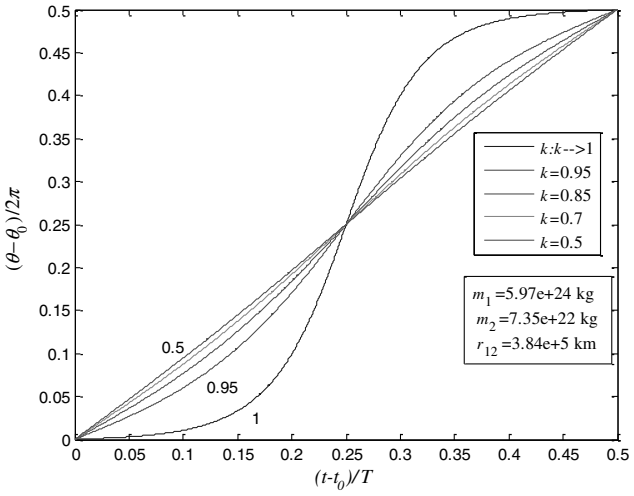

Fig. 4 Angular position behavior of suppositional circular motion.

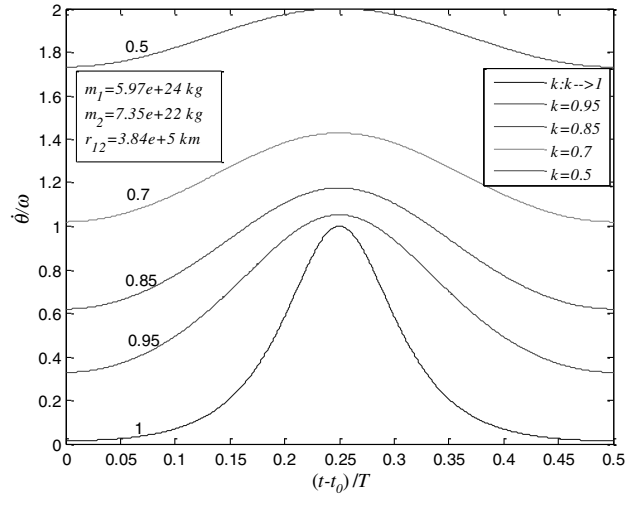

Fig. 5 Angular velocity behavior of suppositional circular motion.

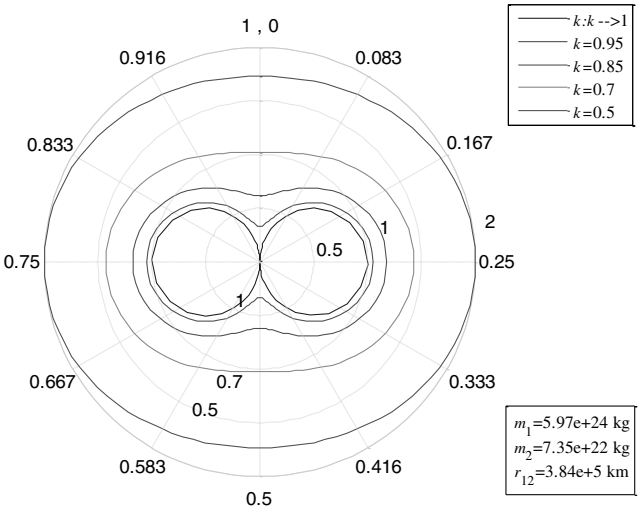

Fig. 6 Phase space polar trajectory of suppositional circular motion.

Figure 4 depicts the normalized angular position against normalized time for half an orbit, whereas Fig. 5 shows the corresponding angular rate response. Clearly, the rate of change of $\theta(t)$ with t is nonuniform and strongly depends on the value of k. As the third body passes through the y'-axis, maximal angular rate occurs, while a minimum occurs on the z'-axis. For the limiting case k: $k \to 1$, the largest variation in angular rate is experienced and the third body approaches a state of rest, in the rotating coordinate system, each time it passes by the z'-axis. For smaller values of k, the $\dot{\theta}(t)$ variation around the orbit is lessened but the averaged and peak $\dot{\theta}(t)$ values increase. For $k < 0.5$, the third body follows essentially uniform speed circular motion. The limiting case k: $k \to 0$ corresponds to precisely constant but infinite speed circular motion.

Finally, Fig. 6 combines the information of Figs. 4 and 5 in a $\theta(t)$ vs $\dot{\theta}(t)$ phase space polar plot in which the radial coordinate is normalized angular velocity and the transverse coordinate is normalized angular position. First, the suppositional motion in Eq. (13) was assumed periodic, and the closed curves in Fig. 6 demonstrate this trait. The varying radius phase plane curves are the signature of nonuniform angular velocity. For k: $k \to 1$, the third body state trajectory in the phase plane consists of two circles forming a lazy figure eight shape. Note the radius of the phase plane trajectory approaches zero for $[\theta(t) - \theta_0]/2\pi = 0$ and 0.5 (z'-axis passage) while for $[\theta(t) - \theta_0]/2\pi = 0.25$ and 0.75 (y'-axis passage) maximum radius values occur. As k is reduced, the phase space closed trajectory transitions from a pinched oval shape to a flattened oval shape. For k: $k \to 0$, the trajectory approaches a constant but infinite radius oval (i.e., circular).

The suppositional motion outlined here and displayed in Fig. 2 is classified as retrograde motion, because the relative angular momentum vector points along the negative x-axis, or because the motion from the z'-axis to the y'-axis follows a left-hand rule. A complete set of identical results exists for direct motion. If the circular motion is in the opposite sense, from the z'-axis to the $-y'$-axis, and the direction of the angular position variable $\theta(t)$ is reversed along with the supposition $x(t) = d_x$, $y(t) = -a\sin\{\theta\}$, $z = a\cos\{\theta\}$, Eq. (19) is easily derived. Applying the transformation $\phi(t) = \theta(t) - \pi/2$ leads to Eq. (21), and all results therefrom.

IV. Initial Condition and Motion Constraints

Certain restrictions on the initial condition pair θ_0 and $\dot{\theta}_0$ exist within the suppositional motion theory. Equation (22) gives the value of the modulus of the elliptic integral in terms of the initial states of the motion. The value of the modulus k is constrained by the following mathematical inequality:

$$k^2 < 1 \tag{30}$$

Substituting from Eq. (22) into Eq. (30) leads to the following inequality:

$$\omega^2 \sin^2\{\theta_0\} < \dot{\theta}_0^2 \tag{31}$$

By using Eqs. (17) and (18), this inequality becomes

$$C_0 > 0 \tag{32}$$

$$C < \omega^2 d_x^2 + 2G\left(\frac{m_1}{\rho_1} + \frac{m_2}{\rho_2}\right) \tag{33}$$

The right-hand side of Eq. (33) is a function of both a and d_x, and it represents an upper limit on the Jacobi constant, C_u, corresponding to certain combinations of a and d_x. This condition is not only a mathematical relation but a physical constraint on the behavior of the dynamical system in the dimensional space.

Figure 7 shows the upper limit (the right-hand side of Eq. (33)) on the nondimensional Jacobi constant as a function of normalized orbit radius for a family of normalized $y'z'$-plane locations. The CRTBP parameters are selected for the Earth–moon system merely used as an example. For certain values for the orbit size and motion plane, possible values for the Jacobi constant must lie below the corresponding curve in Fig. 7. From another perspective, whatever the initial conditions are, they must yield a Jacobi constant which falls within the admissible region in Fig. 7. The admissible region is characterized by all θ_0 and $\dot{\theta}_0$ or C_0, which satisfy Eqs. (32) and (33). For example, for a given initial angle and a particular CRTBP characterization, the initial rate must exceed a threshold for suppositional circular motion to exist. For the center plane ($d_x = 0$) and small orbits ($a < r_{12}$) a wide range of potential C levels exist, whereas for off center planes the allowable C range is significantly less. For large orbits ($a > r_{12}$), all planes in Fig. 7 yield approximately the same potential C range. These trends are a consequence of the manner in which a and d_x influence the right-hand side of Eq. (33). All curves in Fig. 7 appear to intersect precisely at the point $(a, C) = (r_{12}, 2\omega^2 r_{12}^2)$, but this appearance is an artifact of highly unbalanced primary masses ($m_2 \ll m_1$) for the Earth–moon case.

Equations (28) and (29) give the totality of the motion in this analysis. Recalling that for general motion in a plane perpendicular to the x-axis, the phase space is described by the elements of the vector $[y, z, \dot{y}, \dot{z}]$. The motion is completely determined by the initial conditions $[y_0, z_0, \dot{y}_0, \dot{z}_0]$, as the equations of motion are numerically integrated from this point. Under the suppositional theory, the equivalent vector is $[d_x, a, \theta_0, \dot{\theta}_0]$, but the Jacobi integral equation [Eq. (16)] evaluated at $t = t_0$ represents a restriction on the initial

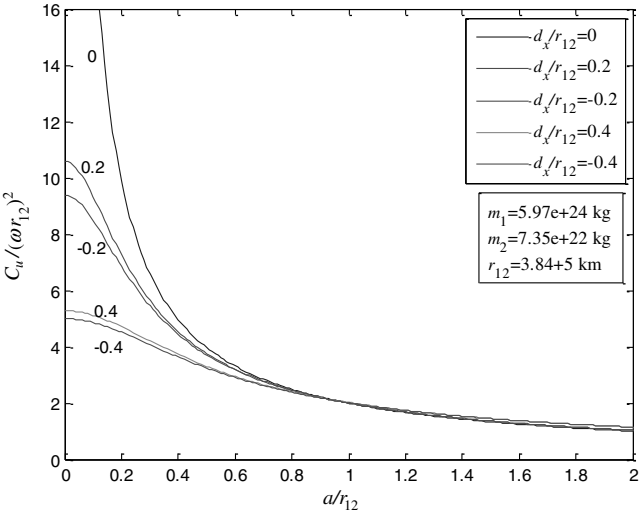

Fig. 7 Upper limit for Jacobi constant for suppositional circular motion.

conditions. This means the four initial conditions are not completely arbitrarily chosen. Once three of the initial conditions are chosen, the fourth one is calculated from the Jacobi integral equation for a given value of C. In other words the Jacobi integral equation is reformulated as follows:

$$f(d_x, a, \theta_0, \dot{\theta}_0) = C \tag{34}$$

Equation (34) represents an algebraic relation between the four initial conditions, which could be used as follows. Parameters d_x and a could be specified, leaving, for a particular C, a relation for $\dot{\theta}_0$ in terms of θ_0, or vice versa. Additionally, if k was specified, Eqs. (22) and (34) would leave two equations for the two dependent parameters θ_0, $\dot{\theta}_0$.

With a completely different perspective, Eq. (16) sets a basis for the principle of accessible and forbidden regions of motion for the third body within the theoretic supposition, because the magnitude square of the angular velocity of the third body must be equal to or greater than zero. For zero $\dot{\theta}(t)$ the suppositionally modified Jacobi integral equation constitutes curves of zero velocity or what is known as equipotential curves. The governing relation is

$$\sin^2\{\theta\} + \frac{1}{\omega^2 a^2}\left\{\omega^2 d_x^2 + 2G\left(\frac{m_1}{\rho_1} + \frac{m_2}{\rho_2}\right) - C\right\} = 0 \tag{35}$$

These curves are parameterized by the Jacobi constant which can be determined by the initial conditions as previously indicated. For a certain C, Eq. (35) is used to solve for θ as a function of a.

Results from this effort are contained in Fig. 8, which shows a family of level curves parameterized by nondimensional C for the center plane location passing through the CRTBP mass center for the example Earth–moon system. The curves of zero velocity consist of two types depending on the value of C. For lower values of C, a pair of opposing trough shaped curves that open vertically exist. These curves tend to constrain the accessible region of motion from the top and bottom, or along the z'-axis. In Fig. 8, the center, left, and right regions correspond to real $\dot{\theta}$, whereas the top and bottom regions yield imaginary $\dot{\theta}$. For higher values of C, a pair of nearly vertical curves offset from the center exists along with an oval shaped curve near the center. These curves disallow motion in the intermediate regions (imaginary $\dot{\theta}$) but leave large regions to the left and right along with the smaller enclosed regions near the center for allowable motion (real $\dot{\theta}$). The accessible region corresponding to real $\dot{\theta}$ for $C = 4\omega^2 r_{12}^2$ is hush marked in gray. Note this region lies within the accessible region for the $C = 3.4\omega^2 r_{12}^2$ curve. Thus, as C increases the accessible region of motion decreases in size. To see the effect of another $y'z'$-plane location, Fig. 9 shows the level curves for a plane passing through the collinear libration point L_1 (Battin [2] definition)

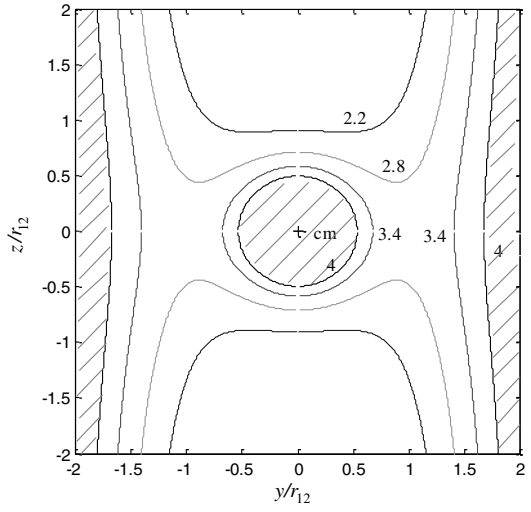

Fig. 8 Zero velocity curves in $y'z'$-plane located at center of mass.

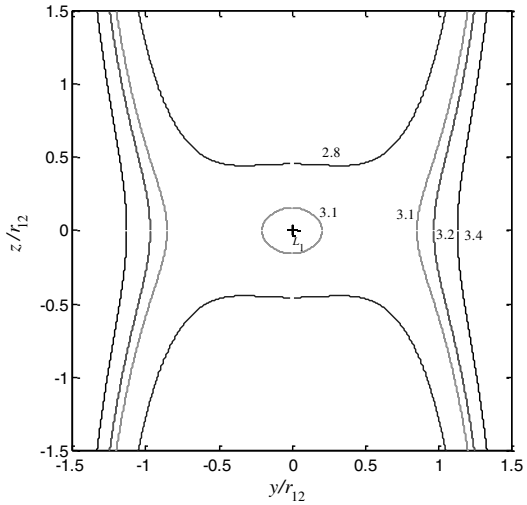

Fig. 9 Zero velocity curves in $y'z'$-plane located at L_1 point.

for the Earth–moon system. Overall, the topological structure in Fig. 9 is similar to Fig. 8. The major difference is that at L_1 the regions of admissible motion, for the same potential level, are smaller than for the center plane case.

The suppositional theory is exclusively circular motion. Thus, the main information extracted from Fig. 8 is the maximum allowable orbit size a for a given C and d_x. For example, the largest accessible radius for $C = 4\omega^2 r_{12}^2$ and $d_x = 0$ is $a = 0.497 r_{12}$. Constant C and the maximum allowable a tend to be inversely proportional. In Fig. 8 the largest radius orbit allowed is always tangent to the zero velocity curves at $y' = 0$ or where the curves cross the z'-axis. To show this, interpret Eq. (35) as the implicit function $a = f(\theta)$. The condition $\mathrm{d}a/\mathrm{d}\theta = 0$ can be used to determine critical values $\theta = \theta_*$ where $a = a_{\min}$, $a = a_{\max}$. For computation, use the explicit function $\theta = f'(a)$ and invert the resulting expression for $\mathrm{d}\theta/\mathrm{d}a$ yielding

$$\frac{\mathrm{d}a}{\mathrm{d}\theta} = -\frac{\omega^2 a^2 \sin\{\theta\}\cos\{\theta\}}{\omega^2 a \sin^2\{\theta\} + G\{m_1 \frac{\mathrm{d}}{\mathrm{d}a}(\frac{1}{\rho_1}) + m_2 \frac{\mathrm{d}}{\mathrm{d}a}(\frac{1}{\rho_2})\}} \tag{36}$$

Applying the extremum condition to Eq. (36) results in

$$\frac{\mathrm{d}a}{\mathrm{d}\theta} = 0 \Rightarrow \theta_* = 0, \qquad \pm\pi \quad \text{or} \quad \theta_* = \pm\frac{\pi}{2} \tag{37}$$

Determination of extremum type requires examination of $\mathrm{d}^2a/\mathrm{d}\theta^2$. Differentiation of Eq. (36) followed with evaluation at $\theta = \theta_*$ gives an expression for the second derivative:

$$\left.\frac{\mathrm{d}^2 a}{\mathrm{d}\theta^2}\right|_{\theta=\theta_*} = -\frac{\omega^2 a^2[\cos^2\{\theta_*\} - \sin^2\{\theta_*\}]}{\omega^2 a \sin^2\{\theta_*\} + G\{m_1 \frac{\mathrm{d}}{\mathrm{d}a}(\frac{1}{\rho_1}) + m_2 \frac{\mathrm{d}}{\mathrm{d}a}(\frac{1}{\rho_2})\}} \tag{38}$$

At $\theta_* = 0, \pm\pi$, the second derivative simplifies to

$$\left.\frac{\mathrm{d}^2 a}{\mathrm{d}\theta^2}\right|_{\theta_*=0,\pm\pi} = \frac{\omega^2 a}{G\{\frac{m_1}{\rho_1^3} + \frac{m_2}{\rho_2^3}\}} > 0 \tag{39}$$

revealing $a = a_{\min}$. At $\theta_* = \pm\pi/2$, the second derivative simplifies to

$$\left.\frac{d^2 a}{\mathrm{d}\theta^2}\right|_{\theta_*=\pm\pi/2} = \frac{\omega^2 a}{G\{m_1(\frac{1}{r_{12}^3} - \frac{1}{\rho_1^3}) + m_2(\frac{1}{r_{12}^3} - \frac{1}{\rho_2^3})\}} \tag{40}$$

Both $a_{\min}$ and $a_{\max}$ can potentially occur here, depending on the value of a. Both θ_* cases are observable in Fig. 8, however, only the case of $\theta_* = 0\ \pm\pi$ has relevant meaning.

To determine $a_{\min}$ corresponding to $\theta_* = 0$, $\pm\pi$ substitute the critical θ value in Eq. (35) and solve for a from

$$\omega^2 d_x^2 + 2G\left(\frac{m_1}{\rho_1} + \frac{m_2}{\rho_2}\right) - C = 0 \tag{41}$$

Note $a_{\min}$ becomes an upper limit, a_u, on the allowable orbit radius ($a_u = a_{\min}$). For computational advantages, Eq. (41) can be converted to the polynomial equation

$$\begin{aligned}&\frac{1}{2}\mathcal{X}^2[\delta_1^2+\alpha^2][\delta_2^2+\alpha^2]\\&\quad\times\left\{\frac{1}{8}\mathcal{X}^2[\delta_1^2+\alpha^2][\delta_2^2+\alpha^2]-\mu_1^2[\delta_1^2+\alpha^2]-\mu_2^2[\delta_2^2+\alpha^2]\right\}\\&\quad+\{\mu_1^2[\delta_1^2+\alpha^2]-\mu_2^2[\delta_2^2+\alpha^2]\}^2=0\end{aligned} \tag{42}$$

where

$$\begin{aligned}\delta_1 &= \frac{d_x}{r_{12}} + \mu_1 \qquad \mu_1 = \frac{m_1}{m_1+m_2} \qquad \mathrm{X} = \frac{C}{\omega^2 r_{12}^2} - \frac{d_x^2}{r_{12}^2}\\ \delta_2 &= \frac{d_x}{r_{12}} - \mu_2 \qquad \mu_2 = \frac{m_2}{m_1+m_2} \qquad \alpha = \frac{a}{r_{12}}\end{aligned} \tag{43}$$

In contrast, substituting $\theta_* = \pm\pi/2$ in Eq. (35) yields an expression from which $a_{\min}$ or $a_{\max}$ can be found depending on the sign of $\mathrm{d}^2a/\mathrm{d}\theta^2$ from Eq. (40).

$$\omega^2 a^2 + \omega^2 d_x^2 + 2G\left(\frac{m_1}{\rho_1} + \frac{m_2}{\rho_2}\right) - C = 0 \tag{44}$$

An equivalent polynomial equation is

$$\begin{aligned}&\frac{1}{2}[\mathcal{X}-\alpha]^2[\delta_1^2+\alpha^2][\delta_2^2+\alpha^2]\\&\quad\times\left\{\frac{1}{8}[\mathcal{X}-\alpha]^2[\delta_1^2+\alpha^2][\delta_2^2+\alpha^2]-\mu_1^2[\delta_1^2+\alpha^2]-\mu_2^2[\delta_2^2+\alpha^2]\right\}\\&\quad+\{\mu_1^2[\delta_1^2+\alpha^2]-\mu_2^2[\delta_2^2+\alpha^2]\}^2=0\end{aligned} \tag{45}$$

Here $a_{\max}$ becomes the lower limit a_l, and $a_{\min}$ is the upper limit a_u, on the allowable orbit radius ($a_1 = a_{\max}$, $a_u = a_{\min}$).

Figure 10 shows the upper limit on the nondimensional orbit radius as a function of normalized Jacobi constant for a family of $y'z'$-plane locations for the example Earth–moon system. For certain values for the Jacobian potential level and motion plane, possible values for the orbit radius must lie below the corresponding curve in Fig. 10. For both center plane ($d_x = 0$) and off center planes ($d_x \neq 0$), and low potential levels ($C < 2\omega^2 r_{12}^2$), a wide range of potential circular orbits exist, whereas for high-potential levels ($C > 2\omega^2 r_{12}^2$) the allowable a range is significantly less. In this latter region, conditions for existence of center plane orbits are always

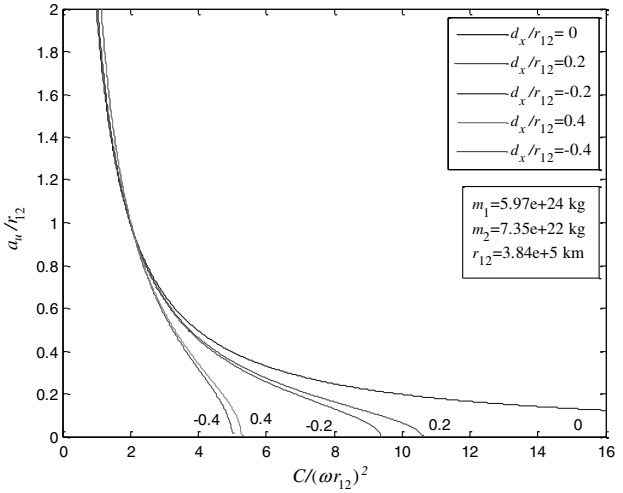

Fig. 10 Upper limit for radius for suppositional circular motion.

Table 1 Quantitative constraints of suppositional and exact zero velocity curves

Normalized Jacobi constant	Normalized orbit radius upper limit	
	Suppositional	Exact
$C/(\omega r_{12})^2$	a_u/r_{12}	a_u/r_{12}
2.2	0.9054	0.9054
2.8	0.7106	0.7106
3.4	0.5846	0.5846
4	0.4965	0.4965

satisfied, but off center plane orbits may or may not exist depending on the value of C. Inspection of Figs. 7 and 10 reveals identical trends because the limiting cases in Eq. (33) and (41) are equivalent. An implication from this equivalence is the nonnegative velocity magnitude square constraint (accessible motion space bounded by zero velocity curves) is one and the same with the less than unity modulus constraint (admissible function space bounded by elliptic integral existence).

An interesting study is to assess consistency of the suppositional zero velocity curves from Eq. (35) with exact zero velocity curves computed from Eq. (11) with $v = 0$. After computing the exact level curves, and comparing them with the suppositional level curves shown in Fig. 8 for the center plane passing through the CRTBP mass center, for the example Earth–moon system no differences were found. Perfect correlation between the exact and suppositional curves exists. Further, the constraints imposed on the suppositional planar orbit (not the true orbit which repeatedly penetrates this plane) by the two sets of curves are also in precise agreement. Table 1 shows a comparison of allowable circular orbit radii from both the suppositional curves and the exact curves for the specific cases shown in Fig. 8. For example, at $C = 4\omega^2 r_{12}^2$ the largest circular orbit that would lie within the boundaries would have a radius of $a = 0.4965 r_{12}$. This orbit would touch the suppositional and exact boundaries at the point $(y/r_{12}, z/r_{12}) = (0, 0.4965)$.

To show how this perfect correlation exists, consider Eq. (11) with $v = 0$ and $x = d_x$:

$$\omega^2 y^2 + \omega^2 d_x^2 + 2G\left(\frac{m_1}{\rho_1} + \frac{m_2}{\rho_2}\right) - C = 0 \tag{46}$$

Within ρ_1 and ρ_2 the $y^2 + z^2$ term can be replaced by r^2 where r denotes the radius to a point lying on the exact zero velocity curve in the $y'z'$-plane. Equation (46) represents the implicit function $r = f(y)$. The condition $\mathrm{d}r/\mathrm{d}y = 0$ yields critical values $y = y_*$ where $r = r_{\min}$, $r = r_{\max}$. For computation, use the explicit function $y = f'(r)$ and invert $\mathrm{d}y/\mathrm{d}r$ giving

$$\frac{\mathrm{d}r}{\mathrm{d}y} = \frac{\omega^2 y}{Gr\left(\frac{m_1}{\rho_1^3} + \frac{m_2}{\rho_2^3}\right)} \tag{47}$$

$$\frac{\mathrm{d}r}{\mathrm{d}y} = 0 \Rightarrow y_* = 0 \tag{48}$$

Computing a second derivative and evaluating at $y = y_*$ gives

$$\left.\frac{\mathrm{d}^2 r}{\mathrm{d}y^2}\right|_{y=y^*} = \frac{\omega^2}{Gr\left(\frac{m_1}{\rho_1^3} + \frac{m_2}{\rho_2^3}\right)} > 0 \tag{49}$$

$$\left.\frac{\mathrm{d}^2 r}{\mathrm{d}y^2}\right|_{y=y^*} > 0 \Rightarrow r = r_{\min} \tag{50}$$

Note $r_{\min}$ becomes an upper limit r_u on the allowable orbit radius ($r_u = r_{\min}$). The equation determining the upper limit r_u is obtained by substituting $y = y_*$ in Eq. (46). The resulting expression matches Eq. (41), hence the perfect correlation.

V. Suppositional Motion Accuracy

Equation (28) represents an exact integration of Jacobi's integral equation under the supposition that $x(t) = d_x$ and $\dot{x}(t) = 0$ are strictly maintained. Unfortunately, this condition is not met. Recall the equations of motion in Eq. (10) with the right-hand sides fully expanded:

$$\ddot{x} - 2\omega\dot{y} = \omega^2 x - \frac{Gm_1(x - x_1)}{[(x - x_1)^2 + y^2 + z^2]^{3/2}} - \frac{Gm_2(x - x_2)}{[(x - x_2)^2 + y^2 + z^2]^{3/2}} \tag{51a}$$

$$\ddot{y} + 2\omega\dot{x} = \omega^2 y - \frac{Gm_1 y}{[(x - x_1)^2 + y^2 + z^2]^{3/2}} - \frac{Gm_2 y}{[(x - x_2)^2 + y^2 + z^2]^{3/2}} \tag{51b}$$

$$\ddot{z} = -\frac{Gm_1 z}{[(x - x_1)^2 + y^2 + z^2]^{3/2}} - \frac{Gm_2 z}{[(x - x_2)^2 + y^2 + z^2]^{3/2}} \tag{51c}$$

Applying the suppositional motion from Eqs. (13–51) yields

$$-2\omega a\dot{\theta}\cos\{\theta\} = \omega^2 d_x - \frac{Gm_1(d_x - x_1)}{[(d_x - x_1)^2 + a^2]^{3/2}} - \frac{Gm_2(d_x - x_2)}{[(d_x - x_2)^2 + a^2]^{3/2}} \tag{52a}$$

$$a[\ddot{\theta}\cos\{\theta\} - \dot{\theta}^2\sin\{\theta\}] = \omega^2 a\sin\{\theta\} - \frac{Gm_1 a\sin\{\theta\}}{[(d_x - x_1)^2 + a^2]^{3/2}} - \frac{Gm_2 a\sin\{\theta\}}{[(d_x - x_2)^2 + a^2]^{3/2}} \tag{52b}$$

$$-a[\ddot{\theta}\sin\{\theta\} + \dot{\theta}^2\cos\{\theta\}] = -\frac{Gm_1 a\cos\{\theta\}}{[(d_x - x_1)^2 + a^2]^{3/2}} - \frac{Gm_2 a\cos\{\theta\}}{[(d_x - x_2)^2 + a^2]^{3/2}} \tag{52c}$$

Multiplying Eq. (52b) by $\cos\{\theta\}$ and Eq. (52c) by $-\sin\{\theta\}$ and combining leads precisely to Eqs. (18) and (19) and the corresponding analytic solution outlined in Sec. III. This preciseness does not imply that either Eq. (52b) or (52c) individually are satisfied, rather it implies a combination of the two equations (Jacobi's integral equation) is satisfied. However, one equation of motion is precisely satisfied. Transform Eqs. (52b) and (52c) to radial and tangential components:

$$a\dot{\theta}^2 + \omega^2 a\sin^2\{\theta\} = G\left\{\frac{m_1}{\rho_1^3} + \frac{m_2}{\rho_2^3}\right\}a \tag{52d}$$

$$a\ddot{\theta} - \omega^2 a\sin\{\theta\}\cos\{\theta\} = 0 \tag{52e}$$

Substituting Eq. (28) and the derivative of Eq. (29) into Eq. (52e) shows the tangential motion equation is exactly solved by the suppositional motion. Thus, the accuracy to which the assumed circular trajectory satisfies the motion equations reduces to the degree to which Eq. (52a) and (52d) are satisfied.

Equation (52a), with the left-hand side being a function of time and the right-hand side being constant, cannot equate over a finite segment of time. The suppositional motion is incorrect in the strictest mathematical sense. Nevertheless, Eq. (52a) can be interpreted to be satisfied in the following approximate sense. The right-hand side of Eq. (52a), $\partial J/\partial x|_{\text{Supposition}} = J_x(d_x, a)$, is a function of d_x and a. Expanding this function with respect to variable a about the point $a = 0$ yields

$$\begin{aligned} J_x(d_x, a) &= J_x(d_x, a)|_{a=0} + \left.\frac{\partial J_x(d_x, a)}{\partial a}\right|_{a=0} a \\ &\quad + \frac{1}{2}\left.\frac{\partial^2 J_x(d_x, a)}{\partial a^2}\right|_{a=0} a^2 + \dots \\ &= \left(\omega^2 d_x - G\left\{\frac{m_1(d_x - x_1)}{|d_x - x_1|^3} + \frac{m_2(d_x - x_2)}{|d_x - x_2|^3}\right\}\right) + (0)a \\ &\quad + \frac{1}{2}\left(3G\left\{\frac{m_1(d_x - x_1)}{|d_x - x_1|^5} + \frac{m_2(d_x - x_2)}{|d_x - x_2|^5}\right\}\right)a^2 + \dots \end{aligned} \tag{53}$$

If the $y'z'$-plane is selected to pass through any of the three collinear libration points, L_1, L_2, L_3 (Battin [2] definition), the first term in the expansion of the right-hand side of Eq. (52a) becomes zero ($J_x(d_x, 0) = 0$ at $d_x = d_{L_1}(\mu)$, $d_{L_2}(\mu)$, $d_{L_3}(\mu)$, $\mu = \mu_2$). Thus, the right-hand side of Eq. (52a) is approximately zero, assuming $a \ll (d_x - x_i)^2$ for $i = 1, 2$ (zero through second order in a). The left-hand side represents a finite zero mean oscillating perturbation, consisting of an elliptic $\text{sn}(\tau, k)$ and $\text{dn}(\tau, k)$ product [see Eqs. (28) and (29)]. Thus, Eq. (52a) is satisfied, in an averaged sense, for each whole orbit completed by the third body. Further, the maximum error at any specific time in Eq. (52a) is bounded. Planes other than the collinear libration planes can be considered, however, Eq. (52a) will not be correct even in the averaged sense.

To show the averaged property, integrate the left-hand side of Eq. (52a) over a general whole orbit (t: $t_0 \to t_0 + T$, $\theta(t)$: $\theta_0 \to \theta_0 + 2\pi$), or

$$\begin{aligned} [-2\omega\dot{y}]|_{\text{avg}} &= -\frac{2\omega a}{T}\int_{t_0}^{t_0+T} \dot{\theta}(t)\cos\{\theta(t)\}\mathrm{d}t \\ &= -\frac{2\omega a}{T}\sin\{\theta(t)\}\Big|_{t_0}^{t_0+T} = -\frac{2\omega a}{T}\sin\{\theta\}\Big|_{\theta_0}^{\theta_0+2\pi} = 0 \end{aligned} \tag{54}$$

For the bounded property, first differentiate the left-hand side of Eq. (52a), leading to

$$\begin{aligned} \frac{\mathrm{d}[-2\omega\dot{y}]}{\mathrm{d}t} &= -2\omega a\frac{\mathrm{d}}{\mathrm{d}t}[\dot{\theta}(t)\cos\{\theta(t)\}] \\ &= -2\omega a\frac{\mathrm{d}}{\mathrm{d}t}\left[\frac{\omega}{k}\text{dn}(\tau(t), k)\text{sn}(\tau(t), k)\right] \\ &= \frac{2\omega^3 a}{k^2}\text{cn}(\tau(t), k)[1 - 2k^2\text{sn}^2(\tau(t), k)] \end{aligned} \tag{55}$$

where

$$\tau(t) = -\frac{\omega}{k}(t - t_0) + F\left(\frac{\pi}{2} - \theta_0, k\right) \tag{56}$$

Applying the condition for perturbation extremums results in

$$\frac{\mathrm{d}[-2\omega\dot{y}]}{\mathrm{d}t} = 0 \Rightarrow \text{cn}(\tau(t), k) = 0 \quad \text{or} \quad \text{sn}(\tau(t), k) = \frac{1}{\sqrt{2}k} \tag{57}$$

The $\text{cn}(\tau(t), k)$ condition leads to minima and maxima when $k \leq 1/\sqrt{2}$, whereas the condition on $\text{sn}(\tau(t), k)$ corresponds to minima and maxima for $k \geq 1/\sqrt{2}$. Thus, upper and lower bounds on the perturbation are

$$\begin{aligned} [-2\omega\dot{y}]_u &= \frac{2\omega^2 a}{k}\text{dn}(\tau_*, k)\text{sn}(\tau_*, k) \\ [-2\omega\dot{y}]_l &= -\frac{2\omega^2 a}{k}\text{dn}(\tau_*, k)\text{sn}(\tau_*, k) \end{aligned} \tag{58}$$

where

$$\tau_* = \begin{cases} F(\pi/2, k) = K(k) & \text{for } k \le 1/\sqrt{2} \\ F(\sin^{-1}(1/\sqrt{2}k), k) & \text{for } k \ge 1/\sqrt{2} \end{cases} \tag{59}$$

The peak error in Eq. (52a) is proportional to the CRTBP rotation rate squared and the third body orbit radius, and inversely proportional to the modulus. Note the product $\mathrm{dn}(\tau_*, k)\ \mathrm{sn}(\tau_*, k)$ will vary between 0.5 and 1 depending on the value of k.

Now focus attention on Eq. (52d), in which again the left-hand side is time dependent and the right-hand side is time independent. Thus, the suppositional motion is again rigorously incorrect, but can be considered, in certain regions of the dimensional space, approximately correct in the following sense. The left-hand side of Eq. (52d), negative radial acceleration $-a_r$, is greater than zero and is limited from above and below. In certain regions of the xyz space, the right-hand side of Eq. (52d) can be shown to lie between the left-hand side limits. Thus, Eq. (52d) is also satisfied, in a banded sense, for all time, assuming the third body orbit falls within the defined region.

To show the limiting property of the left-hand side of Eq. (52d), substitute the suppositional motion solution yielding

$$\begin{aligned}[-a_r] &= a\dot{\theta}^2(t) + \omega^2 a \sin^2\{\theta(t)\} \\ &= \frac{\omega^2 a}{k^2}[\mathrm{dn}^2(\tau(t), k) + k^2 \mathrm{cn}^2(\tau(t), k)]\end{aligned} \tag{60}$$

Differentiate the left-hand side, leading to

$$\begin{aligned}\frac{\mathrm{d}[-a_r]}{\mathrm{d}t} &= \frac{\omega^2 a}{k^2}\frac{\mathrm{d}}{\mathrm{d}t}[\mathrm{dn}^2(\tau(t), k) + k^2 \mathrm{cn}^2(\tau(t), k)] \\ &= \frac{4\omega^3 a}{k}\mathrm{sn}(\tau(t), k)\mathrm{cn}(\tau(t), k)\mathrm{dn}(\tau(t), k)\end{aligned} \tag{61}$$

Applying the condition for extremums provides

$$\frac{\mathrm{d}[-a_r]}{\mathrm{d}t} = 0 \Rightarrow \mathrm{sn}(\tau(t), k) = 0 \quad \text{or} \quad \mathrm{cn}(\tau(t), k) = 0 \tag{62}$$

The $\mathrm{sn}(\tau(t), k)$ condition leads to maxima, whereas the condition on $\mathrm{cn}(\tau(t), k)$ corresponds to minima. Thus, upper and lower limits on the negative radial acceleration are

$$[-a_r]_u = \omega^2 a\left(\frac{1}{k^2} + 1\right) \qquad [-a_r]_l = \omega^2 a\left(\frac{1}{k^2} - 1\right) \tag{63}$$

To determine the region in which the right-hand side of Eq. (52d) is equal to or greater than the left-hand side lower limit the following necessary condition must hold:

$$\omega^2 a\left(\frac{1}{k^2} - 1\right) \le G\left\{\frac{m_1}{\rho_1^3} + \frac{m_2}{\rho_2^3}\right\} a \tag{64}$$

Using Eqs. (17), (18), and (22), the necessary condition becomes

$$\frac{1}{a}\left\{\omega^2 d_x^2 + 2G\left(\frac{m_1}{\rho_1} + \frac{m_2}{\rho_2}\right) - C\right\} \le G\left\{\frac{m_1}{\rho_1^3} + \frac{m_2}{\rho_2^3}\right\} a \tag{65}$$

For positive Jacobi constants, a sufficient condition ensuring Eq. (65) is

$$\frac{1}{a}\left\{\omega^2 d_x^2 + 2G\left(\frac{m_1}{\rho_1} + \frac{m_2}{\rho_2}\right)\right\} \le G\left\{\frac{m_1}{\rho_1^3} + \frac{m_2}{\rho_2^3}\right\} a \tag{66}$$

or

$$\frac{2}{a}\left\{\frac{1}{2}\omega^2 d_x^2 + U(d_x, a)\right\} \le -U_r(d_x, a) \tag{67}$$

where $U(x, r)$ denotes gravitational potential with dependence on x, and the $y'z'$-plane radius r and $U_r(x, r) = \partial U(x, r)/\partial r$. Equation (67) implies the orbit radius must be below a certain threshold to have the right-hand side of Eq. (52d) above the left-hand side lower limit. Suppositional $y'z'$-planes close to the center plane ($d_x = 0$) will reduce this threshold. Regions in which the right-hand side of Eq. (52d) is equal to or less than the left-hand side upper limit are determined by the necessary condition

$$G\left\{\frac{m_1}{\rho_1^3} + \frac{m_2}{\rho_2^3}\right\} a \le \omega^2 a\left(\frac{1}{k^2} + 1\right) \tag{68}$$

Using Eqs. (17), (18), and (22), the necessary condition becomes

$$\begin{aligned}&G\left\{\frac{m_1}{\rho_1^3} + \frac{m_2}{\rho_2^3}\right\} a \\ &\quad \le \omega^2 a\left[2 + \frac{1}{\omega^2 a^2}\left(\omega^2 d_x^2 + 2G\left\{\frac{m_1}{\rho_1} + \frac{m_2}{\rho_2}\right\} - C\right)\right]\end{aligned} \tag{69}$$

For C values maintaining Eq. (33) a sufficient condition ensuring Eq. (69) is

$$G\left\{\frac{m_1}{\rho_1^3} + \frac{m_2}{\rho_2^3}\right\} a \le 2\omega^2 a \tag{70}$$

or

$$-U_r(d_x, a) \le 2\omega^2 a \tag{71}$$

Equation (71) implies the orbit radius must be above a certain threshold to have the right-hand side of Eq. (52d) below the left-hand side upper limit.

Overall, the suppositional circular solution can be described as strictly correct in only one axis and approximately correct (bounded averaged and banded) in the other axes. Of course in numerical propagation error in Eq. (52a) or (52d) will spill over to Eq. (52e).

VI. Iterated Solution Correction

In practice, the supposed planar circular motion solution, applicable to any restricted three-body system, may only be accurate over a short arc of the true 3-D orbit. Fortunately, the mathematical structure of Eq. (51) allows for an iterative analytical approximate procedure to correct the suppositional motion results. Table 2 outlines the iterative perturbation like procedure. Under a motion supposition for the x-axis, the motion in the remaining axes, y and z, are solved for as in Sec. III using Eqs. (51b) and (51c). These results constitute the base solution: x_b, $y_b(t)$, $z_b(t)$. Now, the base solutions in the y and z-axes are used to solve for a correction to the x-axis base

Table 2 Iterative analytical solution

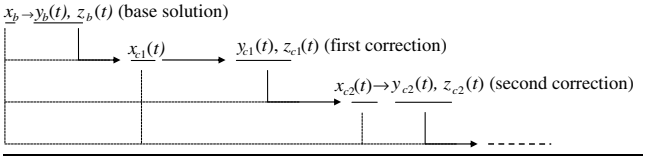

Base solution:	$x(t) \approx \underline{x_b}$ $y(t) \approx \underline{y_b(t)}$ $z(t) \approx \underline{z_b(t)}$
First correction:	$x(t) \approx \{x_b\} + \underline{x_{c1}(t)}$ $y(t) \approx \{y_b(t)\} + \underline{y_{c1}(t)}$ $z(t) \approx \{z_b(t)\} + \underline{z_{c1}(t)}$
Second correction:	$x(t) \approx \{x_b + x_{c1}(t)\} + \underline{x_{c2}(t)}$ $y(t) \approx \{y_b(t) + y_{c1}(t)\} + \underline{y_{c2}(t)}$ $z(t) \approx \{z_b(t) + z_{c1}(t)\} + \underline{z_{c2}(t)}$
...	

solution from Eq. (51a): $x_{c1}(t)$. The total solution is expanded as the base plus first correction and certain approximations are invoked in solving for the correction, including all corrections are small quantities and other sizing restrictions on the y and z-axis base solutions. Next, the x-axis first correction is used in Eqs. (51b) and (51c) to solve for a first correction to the y and z-axis dynamics: $y_{c1}(t)$ and $z_{c1}(t)$. A similar solution procedure is used here and then iterated between $x_{ci}(t)$ and $y_{ci}(t)$, $z_{ci}(t)$. The correction procedure outlined here is also general and does not rely on any specific three-body system.

Base solution results are taken from Sec. III and include

$$x_b = d_x \qquad y_b(t) = a\sin\{\theta(t)\} \qquad z_b(t) = a\cos\{\theta(t)\} \tag{72}$$

where $\sin\{\theta(t)\}$ and $\cos\{\theta(t)\}$ are given in Eq. (28). A correction to x_b is now sought. Substitute

$$x(t) = x_b + x_{c1}(t) \qquad y(t) = y_b(t) \qquad z(t) = z_b(t) \tag{73}$$

into Eq. (51a), which yields

$$\begin{aligned}\ddot{x}_{c1}(t) - 2\omega\dot{y}_b(t) &= \omega^2[x_b + x_{c1}(t)] \\ &- \frac{Gm_1(x_b + x_{c1}(t) - x_1)}{[(x_b + x_{c1}(t) - x_1)^2 + y_b(t)^2 + z_b(t)^2]^{3/2}} \\ &- \frac{Gm_2(x_b + x_{c1}(t) - x_2)}{[(x_b + x_{c1}(t) - x_2)^2 + y_b(t)^2 + z_b(t)^2]^{3/2}}\end{aligned} \tag{74}$$

Expand the nonlinear gravitational terms about the base solution in Eq. (74):

$$\begin{aligned}\ddot{x}_{c1}(t) - 2\omega\dot{y}_b(t) &= \omega^2[x_b + x_{c1}(t)] \\ &- Gm_1\left[\frac{x_b - x_1}{\rho_1^3} + \left\{\frac{1}{\rho_1^3} - \frac{3(x_b - x_1)^2}{\rho_1^5}\right\}x_{c1}(t) + \ldots\right] \\ &- Gm_2\left[\frac{x_b - x_2}{\rho_2^3} + \left\{\frac{1}{\rho_2^3} - \frac{3(x_b - x_2)^2}{\rho_2^5}\right\}x_{c1}(t) + \ldots\right]\end{aligned} \tag{75}$$

To proceed analytically, select $d_x = d_{L_i}(\mu)$ for $i = 1, 2, 3$, cancel out the embedded (approximate bounded-averaged) base solution ($a \ll (d_x - x_i)^2$ for $i = 1, 2$), and delete high-order terms in $x_{c1}(t)$ ($|x_{c1}(t)| \ll \rho_i$ for $i = 1, 2$):

$$\begin{aligned}\ddot{x}_{c1}(t) + \Bigg[-\omega^2 + G\Bigg\{m_1\left(\frac{1}{\rho_1^3} - \frac{3(x_b - x_1)^2}{\rho_1^5}\right) \\ + m_2\left(\frac{1}{\rho_2^3} - \frac{3(x_b - x_2)^2}{\rho_2^5}\right)\Bigg\}\Bigg]x_{c1}(t) = 2\omega\dot{y}_b(t)\end{aligned} \tag{76}$$

$$\begin{aligned}\ddot{x}_{c1}(t) + G\Bigg\{m_1\left(\frac{1}{\rho_1^3} - \frac{3(x_b - x_1)^2}{\rho_1^5} - \frac{1}{r_{12}^3}\right) \\ + m_2\left(\frac{1}{\rho_2^3} - \frac{3(x_b - x_2)^2}{\rho_2^5} - \frac{1}{r_{12}^3}\right)\Bigg\}x_{c1}(t) = 2\omega\dot{y}_b(t)\end{aligned} \tag{77}$$

Depending on the sign of the gravitational coefficient, Eq. (77) represents a stable-unstable forced second order linear time invariant dynamic system. Numerical evaluation of this coefficient over parameters d_x and a confirms very small isolated regions exist, not necessarily at the libration planes, in which the Eq. (77) system is stable. However, the space over parameters d_x and a is dominated by unstable cases, which is consistent with L_1, L_2, L_3 stability analysis [2]. Only the unstable case will be explored further, which is recast as

$$\begin{aligned}&\ddot{x}_{c1}(t) - \lambda_{c1}^2 x_{c1}(t) = 2\omega\dot{y}_b(t) \\ &\lambda_{c1}^2 = \omega^2 - G\Bigg\{m_1\left(\frac{1}{\rho_1^3} - \frac{3(x_b - x_1)^2}{\rho_1^5}\right) \\ &\quad + m_2\left(\frac{1}{\rho_2^3} - \frac{3(x_b - x_2)^2}{\rho_2^5}\right)\Bigg\} > 0\end{aligned} \tag{78}$$

Finally, the forcing function in Eq. (78) is

$$2\omega\dot{y}_b(t) = \frac{2\omega^2 a}{k}\mathrm{sn}(\tau(t), k)\mathrm{dn}(\tau(t), k) \tag{79}$$

In terms of the nome expansion [26], the forcing becomes

$$\begin{aligned}2\omega\dot{y}_b(t) &= \frac{2\omega^2 a}{k}\left[\frac{2\pi}{kK(k)}\sum_{i=0}^{\infty}\frac{q^{i+\frac{1}{2}}}{1 - q^{2i+1}}\sin\left\{\frac{(2i+1)\pi}{2K(k)}\tau(t)\right\}\right] \\ &\bullet\left[\frac{\pi}{2K(k)} + \frac{2\pi}{K(k)}\sum_{j=1}^{\infty}\frac{q^j}{1 + q^{2j}}\cos\left\{\frac{2j\pi}{2K(k)}\tau(t)\right\}\right] \\ &= c_Q\Bigg[\sum_{i=0}^{\infty}Q_i\sin\{\omega_{si}\tau(t)\} \\ &+ \sum_{i=0}^{\infty}\sum_{j=1}^{\infty}Q_{ij}\sin\{\omega_{si}\tau(t)\}\cos\{\omega_{cj}\tau(t)\}\Bigg]\end{aligned} \tag{80}$$

where

$$\begin{aligned}c_Q &= \frac{2\pi^2\omega^2 a}{k^2K^2(k)} \qquad Q_i = \frac{q^{i+\frac{1}{2}}}{1 - q^{2i+1}} \\ Q_{ij} &= 4\frac{q^{i+\frac{1}{2}}}{1 - q^{2i+1}}\frac{q^j}{1 + q^{2j}}, \qquad \omega_{si} = \frac{(2i+1)\pi}{2K(k)} \\ \omega_{cj} &= \frac{2j\pi}{2K(k)} \qquad q = e^{-\pi\frac{K(k')}{K(k)}}, \qquad k' = (1 - k^2)^{1/2}\end{aligned} \tag{81}$$

The homogeneous solution to Eq. (78) is

$$x_{c1H}(t) = A_1 e^{\lambda_{c1}t} + A_2 e^{-\lambda_{c1}t} \tag{82}$$

whereas the nonhomogeneous solution is

$$\begin{aligned}x_{c1NH}(t) &= \sum_{i=0}^{\infty}B_{1i}\sin\{\omega_{si}\tau(t)\} + B_{2i}\cos\{\omega_{si}\tau(t)\} \\ &+ \sum_{i=0}^{\infty}\sum_{j=1}^{\infty}B_{12ij}\sin\{\omega_{si}\tau(t)\}\cos\{\omega_{cj}\tau(t)\} \\ &+ B_{21ji}\sin\{\omega_{cj}\tau(t)\}\cos\{\omega_{si}\tau(t)\}\end{aligned} \tag{83}$$

where

$$\begin{aligned}B_{1i} &= -\frac{c_Q Q_i}{\omega_{si}^2(\frac{\omega}{k})^2 + \lambda_{c1}^2} \qquad B_{2i} = 0 \\ B_{12ij} &= -\frac{c_Q Q_{ij}[(\omega_{si}^2 + \omega_{cj}^2)(\frac{\omega}{k})^2 + \lambda_{c1}^2]}{[(\omega_{si}^2 + \omega_{cj}^2)(\frac{\omega}{k})^2 + \lambda_{c1}^2]^2 - [2\omega_{si}\omega_{cj}(\frac{\omega}{k})^2]^2} \\ B_{21ji} &= \frac{c_Q Q_{ij}[2\omega_{si}\omega_{cj}(\frac{\omega}{k})^2]}{[(\omega_{si}^2 + \omega_{cj}^2)(\frac{\omega}{k})^2 + \lambda_{c1}^2]^2 - [2\omega_{si}\omega_{cj}(\frac{\omega}{k})^2]^2}\end{aligned} \tag{84}$$

Applying the initial conditions $x_{c1}(t_0) = x_{c1_0}$, $\dot{x}_{c1}(t_0) = \dot{x}_{c1_0}$ allow A_1, A_2 to be solved for

$$\begin{aligned}A_1 &= \frac{1}{2\lambda_{c1}}\{\lambda_{c1}e^{-\lambda_{c1}t_0}(x_{c1_0} - \beta_x) + e^{-\lambda_{c1}t_0}(\dot{x}_{c1_0} - \beta_{\dot{x}})\} \\ A_2 &= \frac{1}{2\lambda_{c1}}\{\lambda_{c1}e^{\lambda_{c1}t_0}(x_{c1_0} - \beta_x) - e^{\lambda_{c1}t_0}(\dot{x}_{c1_0} - \beta_{\dot{x}})\}\end{aligned} \tag{85}$$

where

$$\beta_x = \sum_{i=0}^{\infty} B_{1i} \sin\{\omega_{si}\tau(t_0)\} + \sum_{i=0}^{\infty}\sum_{j=1}^{\infty} B_{12ij} \sin\{\omega_{si}\tau(t_0)\}\cos\{\omega_{cj}\tau(t_0)\} + B_{21ji} \sin\{\omega_{cj}\tau(t_0)\}\cos\{\omega_{si}\tau(t_0)\}$$

$$\beta_{\dot{x}} = \sum_{i=0}^{\infty} -B_{1i}\omega_{si}\left(\frac{\omega}{k}\right)\cos\{\omega_{si}\tau(t_0)\} + \sum_{i=0}^{\infty}\sum_{j=1}^{\infty} -B_{12ij}\left(\frac{\omega}{k}\right)[\omega_{si}\cos\{\omega_{si}\tau(t_0)\}\cos\{\omega_{cj}\tau(t_0)\} - \omega_{cj}\sin\{\omega_{si}\tau(t_0)\}\sin\{\omega_{cj}\tau(t_0)\}] - B_{21ji}\left(\frac{\omega}{k}\right)[-\omega_{si}\sin\{\omega_{cj}\tau(t_0)\}\sin\{\omega_{si}\tau(t_0)\} + \omega_{cj}\cos\{\omega_{cj}\tau(t_0)\}\cos\{\omega_{si}\tau(t_0)\}] \tag{86}$$

After collecting results, the complete solution for the x-axis first correction is

$$x_{c1}(t) = A_1 e^{\lambda_{c1}t} + A_2 e^{-\lambda_{c1}t} + \sum_{i=0}^{\infty} B_{1i}\sin\{\omega_{si}\tau(t)\} + \sum_{i=0}^{\infty}\sum_{j=1}^{\infty} B_{12ij}\sin\{\omega_{si}\tau(t)\}\cos\{\omega_{cj}\tau(t)\} + B_{21ji}\sin\{\omega_{cj}\tau(t)\}\cos\{\omega_{si}\tau(t)\} \tag{87}$$

For a general set of initial conditions, and when $x_{c1}(t)$ is added to x_b [see Eq. (73)], the third body will move off the supposition plane with a combined multifrequency oscillatory and aperiodic nature, at least initially whereas the variation from the plane is not excessive, according to Eq. (87). A special class of Eq. (87) solutions, unstable periodic orbits, is also possible for certain initial condition sets. Examples would be libration point halo orbits. To generate this class of motion, homogeneous coefficients A_1, A_2 must be nulled. An initial condition set satisfying this requirement from Eq. (85) is

$$x_{c1_0} = \beta_x \qquad \dot{x}_{c1_0} = \beta_{\dot{x}} \tag{88}$$

Next, corrections to $y_b(t)$ and $z_b(t)$ are addressed. A solution structure of

$$x(t) = x_b + x_{c1}(t) \qquad y(t) = y_b(t) + y_{c1}(t) \qquad z(t) = z_b(t) + z_{c1}(t) \tag{89}$$

is assumed and substituted into Eqs. (51b) and (51c):

$$\ddot{y}_b(t) + \ddot{y}_{c1}(t) + 2\omega\dot{x}_{c1}(t) = \omega^2[y_b(t) + y_{c1}(t)] - \frac{Gm_1(y_b(t)+y_{c1}(t))}{[(x_b + x_{c1}(t) - x_1)^2 + (y_b(t)+y_{c1}(t))^2 + (z_b(t)+z_{c1}(t))^2]^{3/2}} - \frac{Gm_2(y_b(t)+y_{c1}(t))}{[(x_b + x_{c1}(t) - x_2)^2 + (y_b(t)+y_{c1}(t))^2 + (z_b(t)+z_{c1}(t))^2]^{3/2}} \tag{90}$$

$$\ddot{z}_b(t) + \ddot{z}_{c1}(t) = -\frac{Gm_1(z_b(t)+z_{c1}(t))}{[(x_b + x_{c1}(t) - x_1)^2 + (y_b(t)+y_{c1}(t))^2 + (z_b(t)+z_{c1}(t))^2]^{3/2}} - \frac{Gm_2(z_b(t)+z_{c1}(t))}{[(x_b + x_{c1}(t) - x_2)^2 + (y_b(t)+y_{c1}(t))^2 + (z_b(t)+z_{c1}(t))^2]^{3/2}} \tag{91}$$

Gravitational expansion of these relations about the base solution provides

$$\ddot{y}_b(t) + \ddot{y}_{c1}(t) + 2\omega\dot{x}_{c1}(t) = \omega^2[y_b(t) + y_{c1}(t)] - Gm_1\left[\frac{y_b(t)}{\rho_1^3} - \frac{3(x_b - x_1)y_b(t)}{\rho_1^5}x_{c1}(t) + \left\{\frac{1}{\rho_1^3} - \frac{3y_b^2(t)}{\rho_1^5}\right\}y_{c1}(t) - \frac{3y_b(t)z_b(t)}{\rho_1^5}z_{c1}(t) + \ldots\right] - Gm_2\left[\frac{y_b(t)}{\rho_2^3} - \frac{3(x_b - x_2)y_b(t)}{\rho_2^5}x_{c1}(t) + \left\{\frac{1}{\rho_2^3} - \frac{3y_b^2(t)}{\rho_2^5}\right\}y_{c1}(t) - \frac{3y_b(t)z_b(t)}{\rho_2^5}z_{c1}(t) + \ldots\right] \tag{92}$$

$$\ddot{z}_b(t) + \ddot{z}_{c1}(t) = -Gm_1\left[\frac{z_b(t)}{\rho_1^3} - \frac{3(x_b - x_1)z_b(t)}{\rho_1^5}x_{c1}(t) - \frac{3y_b(t)z_b(t)}{\rho_1^5}y_{c1}(t) + \left\{\frac{1}{\rho_1^3} - \frac{3z_b^2(t)}{\rho_1^5}\right\}z_{c1}(t) + \ldots\right] - Gm_2\left[\frac{z_b(t)}{\rho_2^3} - \frac{3(x_b - x_2)z_b(t)}{\rho_2^5}x_{c1}(t) - \frac{3y_b(t)z_b(t)}{\rho_2^5}y_{c1}(t) + \left\{\frac{1}{\rho_2^3} - \frac{3z_b^2(t)}{\rho_2^5}\right\}z_{c1}(t) + \ldots\right] \tag{93}$$

To proceed analytically, cancel out the embedded (approximate banded) base solution and delete high-order terms in $x_{c1}(t)$, $y_{c1}(t)$, $z_{c1}(t)$ ($|x_{c1}(t)|$, $|y_{c1}(t)|$, $|z_{c1}(t)| \ll \rho_i$ for $i = 1, 2$):

$$\ddot{y}_{c1}(t) + \left[-\omega^2 + G\left\{m_1\left(\frac{1}{\rho_1^3} - \frac{3y_b^2(t)}{\rho_1^5}\right) + m_2\left(\frac{1}{\rho_2^3} - \frac{3y_b^2(t)}{\rho_2^5}\right)\right\}\right]y_{c1}(t) + \left[-3G\left\{m_1\frac{y_b(t)z_b(t)}{\rho_1^5} + m_2\frac{y_b(t)z_b(t)}{\rho_2^5}\right\}\right]z_{c1}(t) = -2\omega\dot{x}_{c1}(t) + \left[3G\left\{m_1\frac{(x_b - x_1)y_b(t)}{\rho_1^5} + m_2\frac{(x_b - x_2)y_b(t)}{\rho_2^5}\right\}\right]x_{c1}(t) \tag{94}$$

$$\ddot{z}_{c1}(t) + \left[G\left\{m_1\left(\frac{1}{\rho_1^3} - \frac{3z_b^2(t)}{\rho_1^5}\right) + m_2\left(\frac{1}{\rho_2^3} - \frac{3z_b^2(t)}{\rho_2^5}\right)\right\}\right]z_{c1}(t) + \left[-3G\left\{m_1\frac{y_b(t)z_b(t)}{\rho_1^5} + m_2\frac{y_b(t)z_b(t)}{\rho_2^5}\right\}\right]y_{c1}(t) = \left[3G\left\{m_1\frac{(x_b - x_1)z_b(t)}{\rho_1^5} + m_2\frac{(x_b - x_2)z_b(t)}{\rho_2^5}\right\}\right]x_{c1}(t) \tag{95}$$

Equations (94) and (95) represent two coupled forced second order linear time varying dynamic systems. Taking the y and z-axis base solutions as small with respect to the third body relative position magnitudes ($|y_b(t)|$, $|z_b(t)| \ll \rho_i^{5/2}$ for $i = 1, 2$), Eqs. (94) and (95) simplify to uncoupled time invariant systems:

$$\ddot{y}_{c1}(t) + \left[-\omega^2 + G\left\{\frac{m_1}{\rho_1^3} + \frac{m_2}{\rho_2^3}\right\}\right]y_{c1}(t) = -2\omega\dot{x}_{c1}(t) \tag{96}$$

$$\ddot{y}_{c1}(t) + G\left\{m_1\left(\frac{1}{\rho_1^3} - \frac{1}{r_{12}^3}\right) + m_2\left(\frac{1}{\rho_2^3} - \frac{1}{r_{12}^3}\right)\right\}y_{c1}(t) = -2\omega\dot{x}_{c1}(t) \tag{97}$$

$$\ddot{z}_{c1}(t) + G\left\{\frac{m_1}{\rho_1^3} + \frac{m_2}{\rho_2^3}\right\}z_{c1}(t) = 0 \tag{98}$$

Depending on the sign of the gravitational coefficient in Eq. (97), the y-axis system can be stable or unstable. A condition ensuring the coefficient is positive is $\omega^2 y < -\partial U/\partial y$, or the gravitational acceleration in the y direction is greater than the centripetal acceleration component from a y displacement (assuming $y > 0$). Small radius orbits located between the primary and secondary bodies tend to be y-axis stable, such as small L_1 halo orbits. Small radius orbits lying well outside the CRTBP system (small L_2, L_3 halo orbits) or large radius orbits located anywhere along the x-axis tend to be unstable. The z-axis system in Eq. (98) is always stable. Further note the z-axis system is Coriolis unforced.

Only the stable y-axis case will be explored further. Equations (96) and (98) are recast as

$$\ddot{y}_{c1}(t) + \omega^2_{c1_y} y_{c1}(t) = -2\omega \dot{x}_{c1}(t) \tag{99}$$

$$\omega^2_{c1_y} = -\omega^2 + G\left\{\frac{m_1}{\rho_1^3} + \frac{m_2}{\rho_2^3}\right\} > 0 \tag{100}$$

$$\ddot{z}_{c1}(t) + \omega^2_{c1_z} z_{c1}(t) = 0 \tag{101}$$

$$\omega^2_{c1_z} = G\left\{\frac{m_1}{\rho_1^3} + \frac{m_2}{\rho_2^3}\right\} > 0 \tag{102}$$

The forcing function in Eq. (99), making use of the x-axis first correction in Eq. (87), is

$$\begin{aligned}
-2\omega\dot{x}_{c1}(t) &= -2\omega\Bigg\{A_1\lambda_{c1}e^{\lambda_{c1}t} - A_2\lambda_{c1}e^{-\lambda_{c1}t} \\
&+ \sum_{i=0}^{\infty} -B_{1i}\omega_{si}\left(\frac{\omega}{k}\right)\cos\{\omega_{si}\tau(t)\} \\
&+ \sum_{i=0}^{\infty}\sum_{j=1}^{\infty} -B_{12ij}\left(\frac{\omega}{k}\right)[\omega_{si}\cos\{\omega_{si}\tau(t)\}\cos\{\omega_{cj}\tau(t)\} \\
&- \omega_{cj}\sin\{\omega_{si}\tau(t)\}\sin\{\omega_{cj}\tau(t)\}] \\
&- B_{21ji}\left(\frac{\omega}{k}\right)[-\omega_{si}\sin\{\omega_{cj}\tau(t)\}\sin\{\omega_{si}\tau(t)\} \\
&+ \omega_{cj}\cos\{\omega_{cj}\tau(t)\}\cos\{\omega_{si}\tau(t)\}]\Bigg\} \\
&= c_A\{A_1e^{\lambda_{c1}t} - A_2e^{-\lambda_{c1}t}\} \\
&+ c_{\mathrm{RST}}\Bigg[\sum_{i=0}^{\infty} R_i\cos\{\omega_{si}\tau(t)\} \\
&+ \sum_{i=0}^{\infty}\sum_{j=1}^{\infty} S_{ij}\sin\{\omega_{si}\tau(t)\}\sin\{\omega_{cj}\tau(t)\} \\
&+ T_{ij}\cos\{\omega_{si}\tau(t)\}\cos\{\omega_{cj}\tau(t)\}\Bigg]
\end{aligned} \tag{103}$$

where

$$\begin{aligned}
c_A &= -2\omega\lambda_{c1} \qquad c_{\mathrm{RST}} = \frac{2\omega^2}{k} \qquad R_i = \omega_{si}B_{1i} \\
S_{ij} &= -\omega_{cj}B_{12ij} - \omega_{si}B_{21ji} \qquad T_{ij} = \omega_{si}B_{12ij} + \omega_{cj}B_{21ji}
\end{aligned} \tag{104}$$

The homogeneous solution to Eq. (99) is

$$y_{c1_H}(t) = C_1\sin(\omega_{c1_y}t) + C_2\cos(\omega_{c1_y}t) \tag{105}$$

whereas the nonhomogeneous solution is

$$\begin{aligned}
y_{c1_{NH}}(t) &= D_1e^{\lambda_{c1}t} + D_2e^{-\lambda_{c1}t} + \sum_{i=0}^{\infty} E_{1i}\sin\{\omega_{si}\tau(t)\} \\
&+ E_{2i}\cos\{\omega_{si}\tau(t)\} + \sum_{i=0}^{\infty}\sum_{j=1}^{\infty} E_{11ij}\sin\{\omega_{si}\tau(t)\}\sin\{\omega_{cj}\tau(t)\} \\
&+ E_{22ij}\cos\{\omega_{si}\tau(t)\}\cos\{\omega_{cj}\tau(t)\}
\end{aligned} \tag{106}$$

where

$$D_1 = \frac{c_A A_1}{\lambda_{c1}^2 + \omega^2} \quad D_2 = -\frac{c_A A_2}{\lambda_{c1}^2 + \omega^2} \quad E_{1i} = 0 \quad E_{2i} = \frac{c_{\mathrm{RST}}R_i}{-\omega_{si}^2(\frac{\omega}{k})^2 + \omega^2_{c1_y}} \tag{107a}$$

$$\begin{aligned}
E_{11ij} &= \frac{c_{\mathrm{RST}}[-(\omega_{si}^2 + \omega_{cj}^2)(\frac{\omega}{k})^2 + \omega^2_{c1_y}]S_{ij} - c_{\mathrm{RST}}[2\omega_{si}\omega_{cj}(\frac{\omega}{k})^2]T_{ij}}{[-(\omega_{si}^2 + \omega_{cj}^2)(\frac{\omega}{k})^2 + \omega^2_{c1_y}]^2 - [2\omega_{si}\omega_{cj}(\frac{\omega}{k})^2]^2} \\
E_{22ij} &= \frac{-c_{\mathrm{RST}}[2\omega_{si}\omega_{cj}(\frac{\omega}{k})^2]S_{ij} + c_{\mathrm{RST}}[-(\omega_{si}^2 + \omega_{cj}^2)(\frac{\omega}{k})^2 + \omega^2_{c1_y}]T_{ij}}{[-(\omega_{si}^2 + \omega_{cj}^2)(\frac{\omega}{k})^2 + \omega^2_{c1_y}]^2 - [2\omega_{si}\omega_{cj}(\frac{\omega}{k})^2]^2}
\end{aligned} \tag{107b}$$

Applying the initial conditions $y_{c1}(t_0) = y_{c10}$, $\dot{y}_{c1}(t_0) = \dot{y}_{c1_0}$ allow C_1, C_2 to be solved for

$$\begin{aligned}
C_1 &= \frac{1}{\omega_{c1_y}}[\omega_{c1_y}\sin(\omega_{c1_y}t_0)(y_{c1_0} - \delta_y - \varepsilon_y) \\
&+ \cos(\omega_{c1_y}t_0)(\dot{y}_{c1_0} - \delta_{\dot{y}} - \varepsilon_{\dot{y}})] \\
C_2 &= \frac{1}{\omega_{c1_y}}[\omega_{c1_y}\cos(\omega_{c1_y}t_0)(y_{c1_0} - \delta_y - \varepsilon_y) \\
&- \sin(\omega_{c1_y}t_0)(\dot{y}_{c1_0} - \delta_{\dot{y}} - \varepsilon_{\dot{y}})]
\end{aligned} \tag{108}$$

where

$$\begin{aligned}
\delta_y &= D_1e^{\lambda_{c1}t_0} + D_2e^{-\lambda_{c1}t_0} \\
\delta_{\dot{y}} &= D_1\lambda_{c1}e^{\lambda_{c1}t_0} - D_2\lambda_{c1}e^{-\lambda_{c1}t_0}
\end{aligned} \tag{109}$$

$$\begin{aligned}
\varepsilon_y &= \sum_{i=0}^{\infty} E_{2i}\cos\{\omega_{si}\tau(t_0)\} \\
&+ \sum_{i=0}^{\infty}\sum_{j=1}^{\infty} E_{11ij}\sin\{\omega_{si}\tau(t_0)\}\sin\{\omega_{cj}\tau(t_0)\} \\
&+ E_{22ij}\cos\{\omega_{si}\tau(t_0)\}\cos\{\omega_{cj}\tau(t_0)\} \\
\varepsilon_{\dot{y}} &= \sum_{i=0}^{\infty} E_{2i}\omega_{si}\left(\frac{\omega}{k}\right)\sin\{\omega_{si}\tau(t_0)\} \\
&+ \sum_{i=0}^{\infty}\sum_{j=1}^{\infty} -E_{11ij}\left(\frac{\omega}{k}\right)[\omega_{si}\cos\{\omega_{si}\tau(t_0)\}\sin\{\omega_{cj}\tau(t_0)\} \\
&+ \omega_{cj}\sin\{\omega_{si}\tau(t_0)\}\cos\{\omega_{cj}\tau(t_0)\}] \\
&+ E_{22ij}\left(\frac{\omega}{k}\right)[\omega_{si}\sin\{\omega_{si}\tau(t_0)\}\cos\{\omega_{cj}\tau(t_0)\} \\
&+ \omega_{cj}\cos\{\omega_{si}\tau(t_0)\}\sin\{\omega_{cj}\tau(t_0)\}]
\end{aligned} \tag{110}$$

After collecting results, the complete solution for the y-axis first correction is

$$
\begin{aligned}
y_{c1}(t) &= C_1 \sin(\omega_{c1_y} t) + C_2 \cos(\omega_{c1_y} t) + D_1 e^{\lambda_{c1} t} \\
&+ D_2 e^{-\lambda_{c1} t} + \sum_{i=0}^{\infty} E_{2i} \cos\{\omega_{si}\tau(t)\} \\
&+ \sum_{i=0}^{\infty}\sum_{j=1}^{\infty} E_{11ij} \sin\{\omega_{si}\tau(t)\} \sin\{\omega_{cj}\tau(t)\} \\
&+ E_{22ij} \cos\{\omega_{si}\tau(t)\} \cos\{\omega_{cj}\tau(t)\}
\end{aligned} \tag{111}
$$

For a general set of initial conditions and when $y_{c1}(t)$ is added to $y_b(t)$ [see Eq. (89)], the third body will move off the supposition circle with a combined multifrequency oscillatory and aperiodic nature, at least initially while the variation from the circle is not excessive, according to Eq. (111). A special class of Eq. (111) solutions, unstable periodic orbits, is again possible for certain values of initial conditions. This class of motion occurs when the nonhomogeneous coefficients D_1, D_2 are zero. This condition is achieved by Eq. (88). Finally, a further special class of unstable periodic orbits with no homogeneous frequency content occurs when C_1, C_2 are zero. This condition is achieved when

$$
y_{c1_0} = \varepsilon_y \qquad \dot{y}_{c1_0} = \varepsilon_{\dot{y}} \tag{112}
$$

Being unforced in the Coriolis sense, the z-axis first correction solution is much simpler, having only the homogeneous component. The solution takes the form

$$
z_{c1}(t) = F_1 \sin(\omega_{c1_z} t) + F_2 \cos(\omega_{c1_z} t) \tag{113}
$$

where

$$
\begin{aligned}
F_1 &= \frac{1}{\omega_{c1_z}}[\omega_{c1_z} \sin(\omega_{c1_z} t_0)(z_{c1_0}) + \cos(\omega_{c1_z} t_0)(\dot{z}_{c1_0})] \\
F_2 &= \frac{1}{\omega_{c1_z}}[\omega_{c1_z} \cos(\omega_{c1_z} t_0)(z_{c1_0}) - \sin(\omega_{c1_z} t_0)(\dot{z}_{c1_0})]
\end{aligned} \tag{114}
$$

and the initial conditions are $z_{c1}(t_0) = z_{c1_0}$, $\dot{z}_{c1}(t_0) = \dot{z}_{c1_0}$. For a given set of initial conditions, and when $z_{c1}(t)$ is added to $z_b(t)$ [see Eq. (89)], the third body will again deviate from the supposition circle but with a single-frequency oscillatory nature, assuming the initial conditions are not excessively large, according to Eq. (113). This homogeneous motion is the only motion allowed in the z-axis first correction under the stated assumptions.

This iterative procedure can be extended in a systematic fashion, but a solution through the first correction will suffice here. The overall analytical approximate solution for the third body motion is thus

$$
x(t) = x_b + x_{c1}(t) \qquad y(t) = y_b(t) + y_{c1}(t) \qquad z(t) = z_b(t) + z_{c1}(t) \tag{115}
$$

where x_b, $y_b(t)$, $z_b(t)$ are listed in Eq. (72) and $x_{c1}(t)$, $y_{c1}(t)$, $z_{c1}(t)$ are listed in Eqs. (87), (111), and (113).

VII. L_1 Halo Orbit Example

A periodic L_1 halo orbit for an artificial CRTBP system with $\mu_2 = \mu = 0.04$ is used as a test case for the suppositional motion theory and iterated analytical solution procedure of Secs. III and VI. Howell [27] contains several suitable halo orbits as candidates. In particular, a small $0.17 r_{12} \times 0.076 r_{12}$ sized orbit that undergoes an even smaller variation ($0.046 r_{12}$) in the x-axis is selected for further analysis. Initial conditions for this exact numerical based orbit are given below and correspond to the third body intersecting the xz-plane in the upper quadrants [27]:

$$
\begin{gathered}
x_{h0} = -0.723268 r_{12} \qquad \dot{x}_{h0} = 0 \qquad y_{h0} = 0 \\
\dot{y}_{h0} = 0.198019 \omega r_{12} \qquad z_{h0} = 0.04 r_{12} \qquad \dot{z}_{h0} = 0 \qquad t = t_0
\end{gathered} \tag{116}
$$

The halo orbit geometry is symmetric about the xz-plane. The Jacobi constant for this orbit is $C_h = 3.329168 \omega^2 r_{12}^2$ and the period is $T_h = 2.603/\omega$.

Comparison of the base solution from Sec. VI (suppositional circular motion from Sec. III) with the exact halo orbit, computed from nonlinear simulation, is considered first. Some arbitrariness exists in mapping the exact 3-D orbit initial conditions to the suppositional circular 2-D orbit initial conditions. Initial conditions for the suppositional motion are chosen here as

$$
\begin{gathered}
d_x = -0.74090984286 r_{12}(d_{L_1}) \qquad a = z_{h0} \\
\theta_0 = 0 \qquad \dot{\theta}_0 = \dot{y}_{h0}/z_{h0} \\
t = t_0
\end{gathered} \tag{117}
$$

This a, θ_0, $\dot{\theta}_0$ selection provides a good match to the projected initial halo orbit state, but likely will incur larger error at other locations around the orbit. The base solution modulus value, computed from Eq. (22), with the preceding initial conditions is $k = k_b = 0.198$. The d_x selection at the collinear equilibrium L_1 is based on insights from Sec. V and provides averaged correct x-axis motion as the supposition plane is located in the mean of the motion variation. Figure 11 shows overlay plots of the base and exact solutions. The temporally unsynchronized maximum x, y, z positional errors are $0.0274 r_{12}, 0.0435 r_{12}, 0.0045 r_{12}$. The orbital period error is $1.347/\omega$. The base solution roughly captures the halo orbit yz-plane geometry, but further refinement is required.

Computation of first corrections in the x and y-axes is considered next. Recall no first correction for the z-axis is available. Rather than using the general formulation given in Sec. VI, a truncated version will be considered and to show that the full procedure may not be required for every application. The main departure from the general formulation is truncation of the $2\omega\dot{y}_b(t)$ Coriolis forcing term in Eqs. (79) and (80). A two term nome expansion for the forcing is

$$
\begin{aligned}
\frac{2\omega\dot{y}_b(t)}{(\frac{2\omega^2 a}{k})} &= \frac{\pi^2\sqrt{q}}{kK^2(k)(1-q)}\left[\sin\{v(t)\} + \frac{q}{1+q+q^2}\sin\{3v(t)\}\right. \\
&+ \frac{4q}{1+q^2}\sin\{v(t)\}\cos\{2v(t)\} \\
&\left. + \frac{4q^2}{(1+q+q^2)(1+q^2)}\sin\{3v(t)\}\cos\{2v(t)\}\right]
\end{aligned} \tag{118}
$$

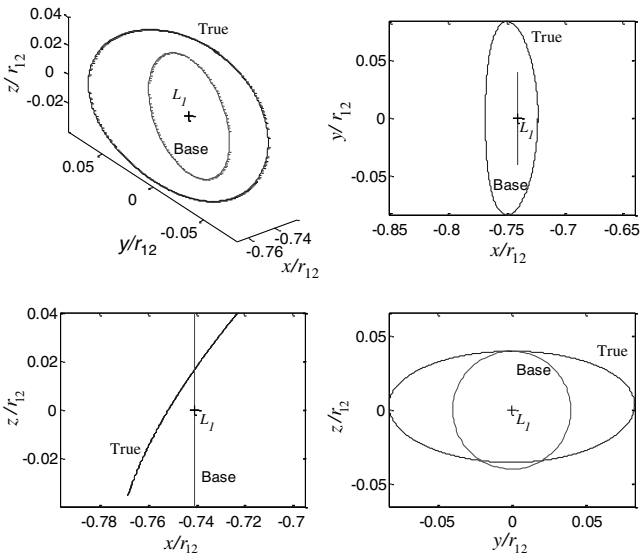

Fig. 11 True and base orbits.

where $v(t) = \pi\tau(t)/2K(k)$. Using the following trigonometric identities

$$\sin\{v(t)\}\cos\{2v(t)\} = \frac{1}{2}\sin\{3v(t)\} - \frac{1}{2}\sin\{v(t)\}$$
$$\sin\{3v(t)\}\cos\{2v(t)\} = \frac{1}{2}\sin\{5v(t)\} + \frac{1}{2}\sin\{v(t)\} \tag{119}$$

Equation (118) is reformulated to

$$\frac{2\omega\dot{y}_b(t)}{(\frac{2\omega^2 a}{k})} = \frac{\pi^2\sqrt{q}}{kK^2(k)(1-q)} \times \left[\left(1 - \frac{2q}{1+q^2} + \frac{2q^2}{(1+q+q^2)(1+q^2)}\right)\sin\{v(t)\} + \left(\frac{q}{1+q+q^2} + \frac{2q}{1+q^2}\right)\sin\{3v(t)\} + \frac{2q^2}{(1+q+q^2)(1+q^2)}\sin\{5v(t)\}\right] \tag{120}$$

Conversion of the forcing signal to a pure sinusoidal nature will simplify calculations. As k decreases the nome q also decreases and the nome dependent harmonic coefficients in Eq. (120) decrease, leaving a simple sine wave which the full expansion would also collapse to. In contrast, when $k \to 1$ the nome dependent harmonic coefficients increase in significance and differences can be expected between the two term and full expansion signals. Figure 12 shows the approximate and exact forcing signal versus dimensionless time for a group of k values. The two term nome formulation should be accurate for $k < 0.85$.

Another smaller departure from the general formulation is retention of the nonzero a^2 term in Eq. (53). This retention leads to an additional constant forcing term in Eq. (78) which improves correction solution accuracy. In this case the solution for the correction in the x-axis is found to be

$$x_{c1}(t) = A_x e^{\lambda_{c1}t} + B_x e^{-\lambda_{c1}t} + C_x + D_x\sin\{v(t)\} + E_x\sin\{3v(t)\} + F_x\sin\{5v(t)\} \tag{121}$$

where A_x and B_x are constants to be determined from initial conditions, and

$$C_x = -\frac{C_{x_{c1}}}{\lambda_{c1}^2}$$
$$C_{x_{c1}} = \omega^2 x_b - \frac{Gm_1(x_b - x_1)}{\rho_1^5} - \frac{Gm_2(x_b - x_2)}{\rho_2^5}$$
$$D_x = -\frac{D_{x_{c1}}}{(\frac{\pi\omega}{2kK(k)})^2 + \lambda_{c1}^2}$$
$$D_{x_{c1}} = \frac{2\omega^2 a}{k}\frac{\pi^2\sqrt{q}}{kK^2(k)(1-q)} \times \left(1 - \frac{2q}{1+q^2} + \frac{2q^2}{(1+q+q^2)(1+q^2)}\right)$$
$$E_x = -\frac{E_{x_{c1}}}{(\frac{3\pi\omega}{2kK(k)})^2 + \lambda_{c1}^2}$$
$$E_{x_{c1}} = \frac{2\omega^2 a}{k}\frac{\pi^2\sqrt{q}}{kK^2(k)(1-q)}\left(\frac{q}{1+q+q^2} + \frac{2q}{1+q^2}\right)$$
$$F_x = -\frac{F_{x_{c1}}}{(\frac{5\pi\omega}{2kK(k)})^2 + \lambda_{c1}^2}$$
$$F_{x_{c1}} = \frac{2\omega^2 a}{k}\frac{\pi^2\sqrt{q}}{kK^2(k)(1-q)}\left(\frac{2q^2}{(1+q+q^2)(1+q^2)}\right) \tag{122}$$

Applying the initial conditions $x_{c1}(t_0) = x_{c1_0}, \dot{x}_{c1}(t_0) = 0$ with $t_0 = 0$ yields

$$x_{c1_0} = A_x + B_x + C_x + D_x - E_x + F_x \qquad 0 = A_x - B_x \tag{123}$$

To remove the nonperiodic terms ($A_x = B_x = 0$) in Eq. (121) the required condition is

$$x_{c1_0} = C_x + D_x - E_x + F_x \tag{124}$$

Equation (124) is equivalent to the first expression in Eq. (88) for the general formulation.

The required condition in Eq. (124) facilitates a correction to the modulus value. The initial position x_{c1_0} is first computed from the halo orbit data as $x_{c1_0} = x_{h_o} - d_x = 0.01764r_{12}$. Observing that coefficients C_x, D_x, E_x, F_x are functions of k [see Eq. (122)], Eq. (124) is reformulated as

$$f(k) - x_{c1_0} = 0 \tag{125}$$

Equation (125) is to be solved for k numerically. Because not all the harmonics are included in the solution, one cannot expect Eq. (125) to be fully satisfied for any value of k. An appropriate value for k, which corresponds to the minimum of the left-hand side magnitude

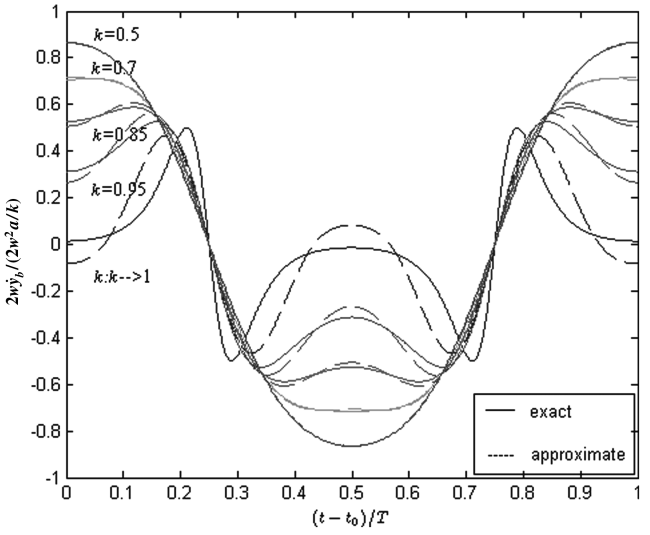

Fig. 12 Approximate and exact forcing signals.

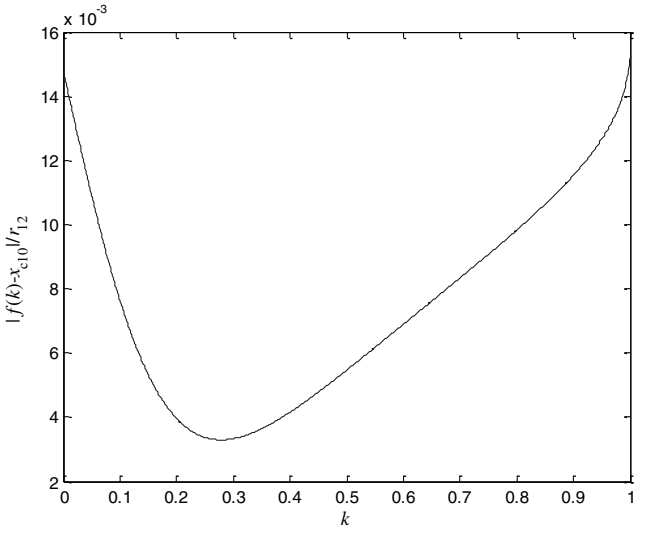

Fig. 13 Equation (125) error vs elliptic modulus.

of Eq. (125), will be considered here. Figure 13 shows the absolute value of the left-hand side of Eq. (125) versus k. The x-axis first correction modulus value corresponding to the minimum Eq. (125) error is $k = k_{x_{c1}} = 0.279$. Finally, the solution for the first correction in the x-axis is written as follows:

$$x_{c1}(t) = C_x + D_x \sin\{v(t)\} + E_x \sin\{3v(t)\} + F_x \sin\{5v(t)\} \tag{126}$$

Because the value of k does not completely satisfy Eq. (125) the initial value x_{c1_0} is automatically adjusted by Eq. (126) when the coefficients are computed from k obtained in Eq. (125).

Using the result from the x-axis to correct $y(t)$, the solution for the y-axis first correction is found to be

$$y_{c1}(t) = A_y \cos\{\omega_{c1_y} t\} + B_y \sin\{\omega_{c1_y} t\} + D_y \cos\{v(t)\} + E_y \cos\{3v(t)\} + F_y \cos\{5v(t)\} \tag{127}$$

where A_y and B_y are constants to be determined from initial conditions, and

$$\begin{aligned} D_y &= \frac{D_{y_{c1}}}{\omega_{c1_y}^2 - (\frac{\pi\omega}{2kK(k)})^2} \qquad & D_{y_{c1}} &= \frac{\pi\omega^2}{kK(k)} D_x \\ E_y &= \frac{E_{y_{c1}}}{\omega_{c1_y}^2 - (\frac{3\pi\omega}{2kK(k)})^2} \qquad & E_{y_{c1}} &= \frac{3\pi\omega^2}{kK(k)} E_x \\ F_y &= \frac{F_{y_{c1}}}{\omega_{c1_y}^2 - (\frac{5\pi\omega}{2kK(k)})^2} \qquad & F_{y_{c1}} &= \frac{5\pi\omega^2}{kK(k)} F_x \end{aligned} \tag{128}$$

The initial conditions, $y_{c1}(t_0) = 0$, $\dot{y}_{c1}(t_0) = \dot{y}_{c1_o}$, $t_0 = 0$, when applied to Eq. (127) and its derivative result in

$$0 = A_y \qquad \dot{y}_{c1_0} = \omega_{c1_y} B_y + \frac{\pi\omega}{2kK(k)} \{D_y - 3E_y + 5F_y\} \tag{129}$$

To eliminate the homogeneous part of the solution ($B_y = 0$), the following condition should be satisfied:

$$\dot{y}_{c1_0} = \frac{\pi\omega}{2kK(k)} (D_y - 3E_y + 5F_y) \tag{130}$$

In the general formulation, Eq. (130) corresponds to Eq. (112).

There appear to be at least three plausible interpretations to the meaning and utilization of Eq. (130) in conjunction with Eqs. (22) and (124). The solution theory in this paper is analytically consistent, implying existence of a single unique k for the exact solution. Because approximations have been invoked and only a single iteration has been considered, a unique k satisfying Eqs. (22), (124), and (130) simultaneously does not exist. The first interpretation is to compute three separate moduli ($k = k_b$, $k = k_{x_{c1}}$, $k = k_{y_{c1}}$) and use them in the appropriate solution components ($k_b \to y_b(t)$ and $z_b(t)$, $k_{x_{c1}} \to x_{c1}(t)$, $k_{y_{c1}} \to y_{c1}(t)$). Moduli k_b and $k_{x_{c1}}$ have already been considered. Modulus $k_{y_{c1}}$ would be computed from Eq. (130) with $\dot{y}_{c1_0} = 0$ because the full halo orbit initial velocity $\dot{y}_{h_o}$ has been previously applied to the base solution [see Eq. (117)]. This interpretation was investigated. Although rigorous solutions to Eq. (130) with $\dot{y}_{c1_0} = 0$ exist for the limiting cases k: $k \to 0$ and $k \to 1$, no other values of k precisely satisfy the required condition. However, broad regions were found in which the right-hand side of Eq. (130) was nearly zero and independent of the value of k, implying the possibility of vastly different values of the three moduli or the insignificance of the Eq. (130) condition. Consequently, this interpretation was abandoned. The second interpretation is to compute a single optimum k ($k = k_b = k_{x_{c1}} = k_{y_{c1}}$) which best satisfies all three equations. The problem formulation would involve unknowns k, x_{c1_0} and the percentage distribution of $\dot{y}_{h_0}$ to initial conditions $\dot{\theta}_0$ and $\dot{y}_{c1_0}$. This interpretation appears overly complicated and was not considered.

The third interpretation, lying somewhere in between the first and second interpretations, is to compute a single optimum k which best satisfies a single equation [Eq. (124), $k = k_{x_{c1}}$]. This single k would then be used consistently throughout all solution components ($k_{x_{c1}} \to y_b(t)$ and $z_b(t)$, $k_{x_{c1}} \to x_{c1}(t)$, $k_{x_{c1}} \to y_{c1}(t)$). Implementation here is simpler and is congruent with numerical differential correction logic in the following sense. With the appropriate value of the modulus determined from Eq. (124), Eq. (130) is used to compute the change in the initial y-axis velocity. Thus, at each step of the iteration process there should be an increment in the initial y-axis velocity. The mechanism of the iterative solution procedure is acting like a differential correction technique. However, this increment in the initial y-axis velocity is not used in the analytical orbit construction process because numerical integration is not employed.

The third interpretation was adopted for this work, and the computation effort was already presented in Fig. 13. Using $k = k_{x_{c1}} = 0.279$ in Eq. (128) to compute coefficients D_y, E_y, F_y, the solution for the first correction in y is

$$y_{c1}(t) = D_y \cos\{v(t)\} + E_y \cos\{3v(t)\} + F_y \cos\{5v(t)\} \tag{131}$$

Care should be taken to avoid resonance forcing singularity in the solution, which occurs when

$$\omega_{c1_y} = \frac{n\pi}{2kK(k)}, \qquad n = 1, 3, 5 \tag{132}$$

Figure 14 shows the dimensionless natural frequency to be avoided as a function of k for the three possible forcing signals parameterized by n.

Figure 15 shows the analytic orbit construction after the first correction iteration using the two term nome expansion with the true orbit. The temporally unsynchronized maximum x, y, z positional errors are $0.0131r_{12}$, $0.0165r_{12}$, $0.0045r_{12}$. Using the true halo orbit dimensions as the reference, the first correction has reduced the maximum positional error in the x-axis from 60% to 28% and in the y-axis from 26% to 9.7%. No change has occurred in the z-axis. Also the period error has reduced to 34% from 52%. The orbital period error is $0.89/\omega$. The corrected orbit has the sloped xz-plane track and the flattened yz-plane closed path signatures commonly exhibited by halo-class orbits. The xz-plane track does not show any significant curvature at this iteration, but the rectilinear track reasonably captures the true motion behavior. Note how coefficient C_x has pushed the track away from the L_1 point. Also note how the D_y coefficient has amplified the distance the third body travels from the x-axis when it traverses from the upper quadrants to the lower quadrants. Significant improvement in the halo orbit prediction is noted in Fig. 15 after one correction iteration. Depending on the application and required accuracy, a second iteration for the analytic solution can be considered. Determination of sufficiency of the required number of corrections can be judged by the respective contributions to the total solution, and the intended application.

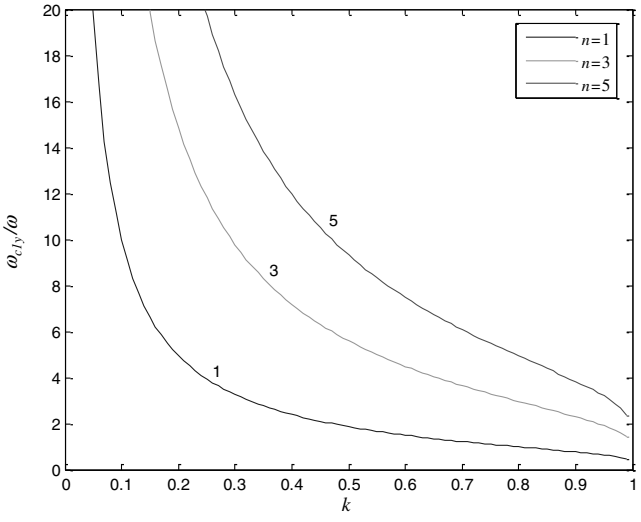

Fig. 14 Natural frequency at singularity conditions.

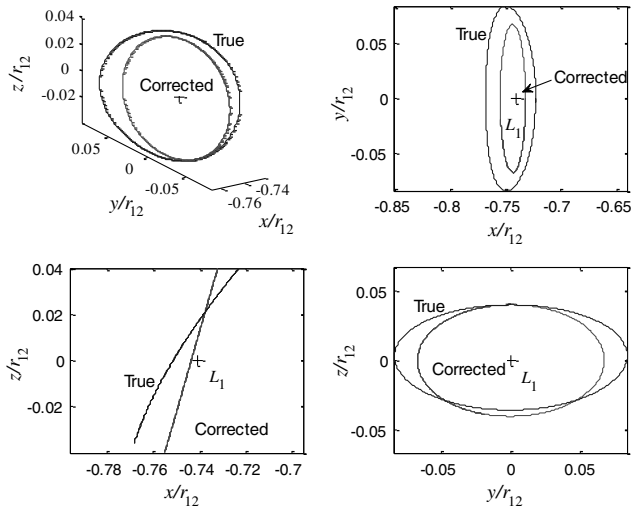

Fig. 15 True and two term once corrected orbit.

Geometry of halo orbits for mission design can be reduced in preliminary studies to the average slope of the xz-plane track, M, and the approximate vertical-to-horizontal aspect ratio of the yz-plane path, A. Suitable definitions for these parameters for the analytic solution displayed in Fig. 15 are

$$M = \frac{z(t_0) - z(t_0 + \frac{k}{\omega}K(k))}{x(t_0) - x(t_0 + \frac{k}{\omega}K(k))} \quad \text{with} \quad \theta_0 = 0, \qquad t_0 = 0 \tag{133}$$

$$A = \frac{z(t_0)}{y(t_0 + \frac{k}{\omega}K(k))} \quad \text{with} \quad \theta_0 = 0, \qquad t_0 = 0 \tag{134}$$

Note $t = 0$ corresponds to $\theta = 0$, whereas $t = (k/\omega)K(k)$ corresponds to $\theta = \pi/2$ rad. Using the analytic results and simplifying by neglecting E_x, F_x, E_y, F_y [$\mathcal{O}(E_x, F_x, E_y, F_y) \ll \mathcal{O}(D_x, D_y)$ holds for the numerical example], the slope and aspect ratio can be expressed symbolically as

$$M(k) = \frac{a}{D_x} = -\frac{(\frac{\pi\omega}{2kK(k)})^2 + \lambda_{c1}^2}{8(\frac{\pi\omega}{2kK(k)})^2 f(q(k))}$$
$$= -\frac{1 + \frac{4}{\pi^2}k^2K^2(k)[1 - \frac{G}{\omega^2}\{m_1(\frac{1}{\rho_1^3} - \frac{3(d_x - x_1)^2}{\rho_1^5}) + m_2(\frac{1}{\rho_2^3} - \frac{3(d_x - x_2)^2}{\rho_2^5})\}]}{8(f(q(k))} \tag{135}$$

$$A(k) = \left(1 + \frac{D_y}{a}\right)^{-1} = \left(1 + \frac{\frac{8\pi\omega^2}{kK(k)}(\frac{\pi\omega}{2kK(k)})^2 f(k)}{[(\frac{\pi\omega}{2kK(k)})^2 - \omega_{c1_y}^2][(\frac{\pi\omega}{2kK(k)})^2 + \lambda_{c1}^2]}\right)^{-1}$$
$$= \left(1 + \frac{\frac{32}{\pi}kK(k)f(k)}{[1 + \frac{4k^2K^2(k)}{\pi^2}\{1 - \frac{G}{\omega^2}\{\frac{m_1}{\rho_1^3} + \frac{m_2}{\rho_2^3}\}\}][1 + \frac{4k^2K^2(k)}{\pi^2}\{1 - \frac{G}{\omega^2}\{m_1(\frac{1}{\rho_1^3} - \frac{3(d_x - x_1)^2}{\rho_1^5}) + m_2(\frac{1}{\rho_2^3} - \frac{3(d_x - x_2)^2}{\rho_2^5})\}\}]}\right)^{-1} \tag{136}$$

where

$$f(q(k)) = \frac{\sqrt{q}}{1 - q}\left(1 - \frac{2q}{1 + q^2} + \frac{2q^2}{(1 + q + q^2)(1 + q^2)}\right) \tag{137}$$

These expressions can be used in various ways. For example, mission sensing or communication objectives may impose certain requirements on a satellite to periodically transit various regions in the three-body spatial system. Given a preliminary set of values for d_x, a, x_{c1_0}, the modulus k can be computed, and from this the halo orbit slope and aspect ratio can be computed. If the orbit does not meet the requirements satisfactorily, sensitivities of M and A with respect to variations in k can be analyzed with Eqs. (135) and (136) for modification purposes. The analytical expressions could also be useful with inverse problems, in which parameters M, A are specified along with d_x to satisfy mission objectives, and Eqs. (135) and (136) are used to compute compatible a, k values. Additionally, Eqs. (135) and (136) could be differentiated with respect to k to identify extremal conditions for slope or aspect ratio. Assuming all assumptions taken in the derivation of the expressions are maintained, Eqs. (135) and (136) could provide physical insight and avoid costly numerical propagation within iterative searches, i.e., when the slope and aspect ratio are preselected and the appropriate orbital parameters are calculated. Even in other numerical differential correction techniques, such as numerically constructing a periodic orbit by finding appropriate initial position-velocity pairs, the supposed orbit may provide a better initial guess than the linearized equation solution, and this affects directly the required computational convergence time. By combining Eqs. (135) and (136) a direct relation between M and A for design purposes can also be derived. Finally, if mission requirements involve time, the orbital period through Eq. (24) can be coupled to the process.

VIII. Exact Circular Motion with Thrust

If the third body is an artificial satellite with an actively controlled propulsion subsystem, such capability can be exploited to render the suppositional motion described in Sec. III exact. Such an orbit could be useful for communications, in situ space measurements, observation platforms, loitering, etc., particularly in regions where natural halo orbits do not exist or are expensive to maintain due to instabilities. The proposed exact circular vertical orbit maintained by thrust would then add a mission design freedom or a potential design alternative. In this section, the required thrust will be calculated and presented in a nondimensional way, such that any user can convert the data to specific fuel/thrust requirements for a specific engine-vehicle system.

Let the accelerative thrust components be denoted by $a_{T_x}, a_{T_y}, a_{T_z}$. The equations of motion [see Eq. (10)] for the third body are altered to

$$\ddot{x} - 2\omega\dot{y} = \frac{\partial J}{\partial x} + a_{T_x} \tag{138a}$$

$$\ddot{y} + 2\omega\dot{x} = \frac{\partial J}{\partial y} + a_{T_y} \tag{138b}$$

$$\ddot{z} = \frac{\partial J}{\partial z} + a_{T_z} \tag{138c}$$

Equation (138a) under the supposition yields

$$a_{T_x} = -2\omega a\dot{\theta}\cos\{\theta\} - J_x(d_x, a) \tag{139}$$

Equations (138b) and (138c), when expanded under the supposition and transformed in the same manner as in Sec. V, give

$$a_{T_r} = a_{T_y}\sin\{\theta\} + a_{T_z}\cos\{\theta\}$$
$$= -a\dot{\theta}^2 - \omega^2 a\sin^2\{\theta\} + G\left\{\frac{m_1}{\rho_1^3} + \frac{m_2}{\rho_2^3}\right\}a \tag{140}$$

$$a_{T_t} = a_{T_y}\cos\{\theta\} - a_{T_z}\sin\{\theta\} = a\ddot{\theta} - \omega^2 a\sin\{\theta\}\cos\{\theta\} \tag{141}$$

where a_{T_r}, a_{T_t} are the accelerative thrust components in the radial and tangential directions. Figure 16 shows the various thrust acceleration components in the suppositional plane $y'z'$-axes and the radial-tangential rt-axes.

The supposition motion solves the governing tangential relation Eq. (141) exactly without need for tangential thrust. Thus,

$$a_{T_t} = a_{T_y}\cos\{\theta\} - a_{T_z}\sin\{\theta\} = 0 \tag{142}$$

For certain regions within the xyz space, the centripetal and gravitational accelerations appearing in the right-hand side of the governing radial expression were shown to be approximately balanced, in a banded sense. At any specified time, to exactly balance these terms and preserve the suppositional motion, the radial thrust acceleration must equal the difference between these centripetal and gravitational terms. By substituting for $\dot{\theta}$ from Jacobi's integral equation under the supposition motion into Eq. (140), the radial accelerative thrust can be expressed as

$$a_{T_r} = a_{T_y}\sin\{\theta\} + a_{T_z}\cos\{\theta\} = -2a\omega^2\sin^2\{\theta\} + c_T \tag{143}$$

where c_T is a constant which depends on the characteristics of the three-body system and the suppositional motion. This constant can be either positive, negative, or zero:

$$c_T = G\left\{\frac{m_1}{\rho_1^3} + \frac{m_2}{\rho_2^3}\right\}a - (a\dot{\theta}_0^2 - \omega^2 a\sin^2\{\theta_0\}) \tag{144}$$

Equation (139) gives the required propulsive x-axis acceleration to maintain planar circular motion for a general $y'z'$-plane. By selecting d_x to coincide with libration points L_1, L_2, or L_3, the thrust requirement simplifies [see Eq. (53)] to

$$a_{T_x} = -2\omega a\dot{\theta}\cos\{\theta\} - \frac{1}{2}\frac{\partial^2 J_x(d_x, a)}{\partial a^2}\bigg|_{a=0} a^2 + \ldots \tag{145}$$

The residual gravitational terms appearing in the right-hand side of Eq. (145) were shown to be small, in a bounded-averaged sense. Thus, the required cylindrical thrust component is dominated by the Coriolis acceleration. Solving Eqs. (142) and (143) simultaneously, the following expressions for the thrust accelerations in the y and z directions become

$$a_{T_y} = [-2\omega^2 a\sin^2\{\theta\} + c_T]\sin\{\theta\} \tag{146}$$

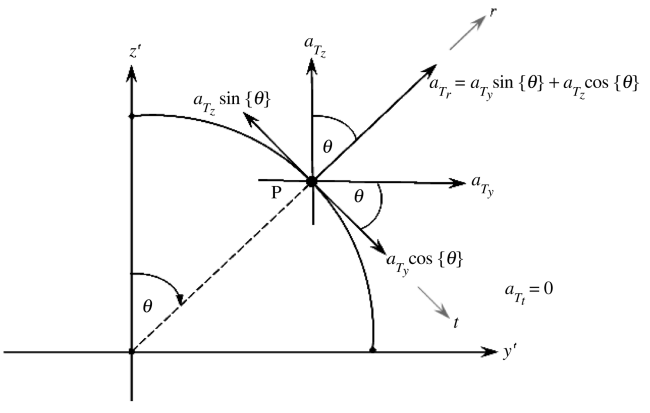

Fig. 16 Exact circular motion with thrust geometry.

$$a_{T_z} = [-2\omega^2 a\sin^2\{\theta\} + c_T]\cos\{\theta\} \tag{147}$$

Figures 17 and 18 show the nondimensional accelerative thrust demands for this special case against normalized time for half an orbit, across a family of elliptic moduli, for the Earth–moon system, using an orbit radius of $a = 0.05r_{12}$. In Fig. 17, all accelerative thrust curves in the radial direction have similar behavior (constant plus elliptic $\mathrm{cn}(\tau(t), k)$ square nature) with time, except the limiting case k: $k \to 1$. In this case, results indicate a sharp reduction in thrust demand at $\theta = n\pi/2$, $n = 1, 3, 5, \ldots$, and between these values thrust can be approximated to be constant. Also note all curves have minimums at $\theta = n\pi/2$, $n = 1, 3, 5, \ldots$ and maximums at $\theta = n\pi$, $n = 0, 1, 2, 3, \ldots$. Further the radial thrust acceleration is nearly always positive. For the considered orbit radius and elliptic moduli values, the gravitational acceleration is larger than the centripetal acceleration, and outward (positive) radial thrust is required to maintain the circular path. Figure 18 shows the thrust acceleration component in the cylindrical direction (x-axis). Note all curves intersect at common points $\theta = n\pi/2, n = 1, 3, 5, \ldots$, at which they all have the same value equaling the constant gravitational part in Eq. (145). With the value of k getting smaller, the thrust in the x direction approaches a cosine wave that is shifted above the zero value. Generally, the required thrust profiles take the shape of a constant plus an elliptic $\mathrm{sn}(\tau(t), k)$ and $\mathrm{dn}(\tau(t), k)$ product. For the considered orbit radius, the second order gravitational attraction that exists in the L_1 libration plane is toward the second primary, thus

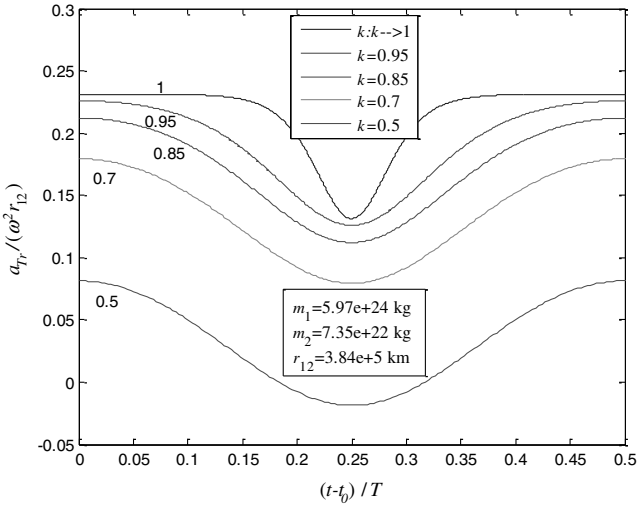

Fig. 17 Radial thrust component vs time.

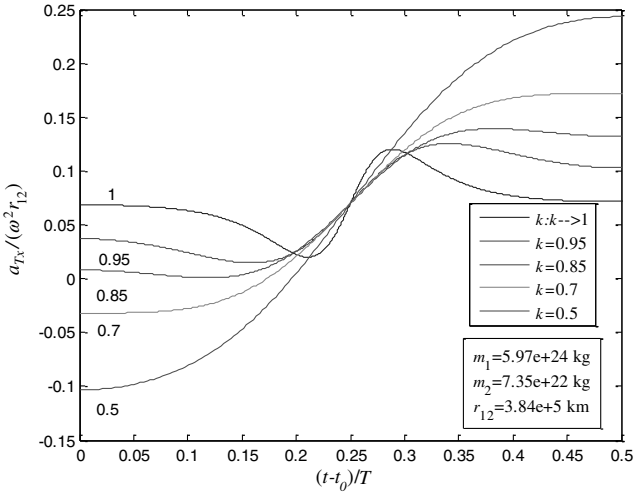

Fig. 18 Cylindrical thrust component vs time.

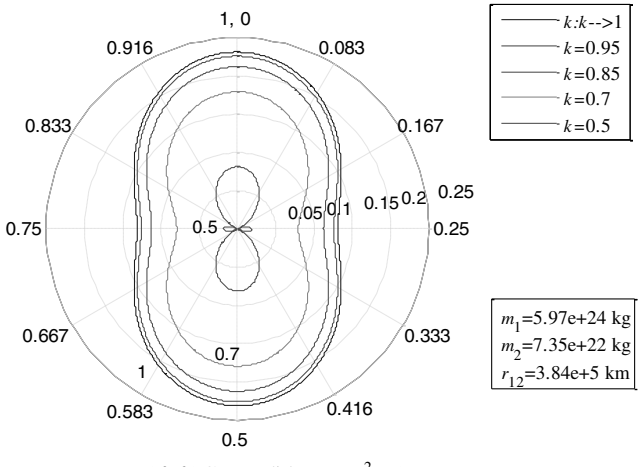

Fig. 19 Radial thrust component vs angle.

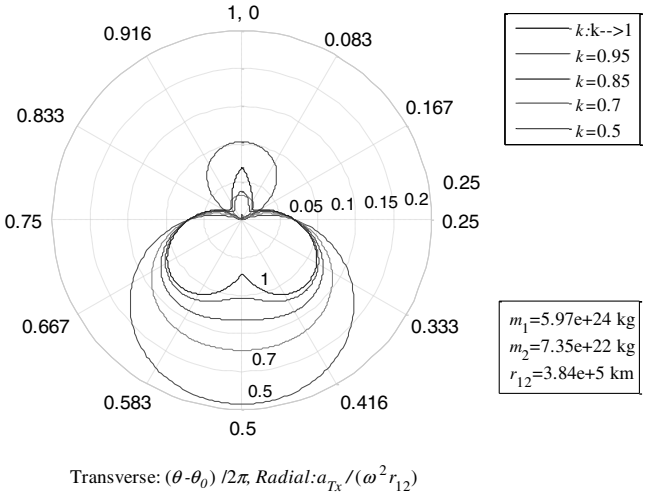

Fig. 20 Cylindrical thrust component vs angle.

requiring a positive (toward the first primary) bias in the cylindrical thrust. Overall the rate of change of a_{T_r}, a_{T_x} is nonuniform and strongly depend on k. The peak values of a_{T_r}, a_{T_x} are also a strong function of k. For the limiting case k: $k \to 1$ in Fig. 18, the smallest peak propulsive acceleration and smallest integrated propulsive acceleration (impulse) are experienced. For smaller values of k, required peak and integrated thrust accelerations to maintain circular motion increase. The case k: $k \to 0$ requires infinite propulsive capability. Opposite but similar trends are noted in Fig. 17. The largest (positive) propulsive demand occurs in the k: $k \to 1$ case. For k: $k \to 0$ the required thrust approaches an infinite negative bias.

Figures 19 and 20 show the nondimensional thrust acceleration against normalized angle. These figures help with visualizing the thrust demands at different locations in the physical coordinates. Figure 19 indicates that the amount of radial thrust in the upper half ($z > 0$) of the orbit is the same as in the lower half of the orbit. Acceleration demand curves are symmetrical with respect to both the y-axis and z-axis. Figure 20 shows that the amount of cylindrical thrust required in the lower half of the orbit is larger than that in the upper half of the orbit. Thrust demand curves are symmetrical with respect to the z-axis but unsymmetrical with respect to the y-axis. In the lower half, the Coriolis acceleration is aligned with the gravitational bias, thus requiring more thrust to maintain planar motion. Figures 17 and 18 showed when thrust components are positive or negative, which is critical for determining the instantaneous direction of the total thrust vector in space. In contrast, Figs. 19 and 20 show only absolute values of thrust at different locations along the orbit. Together the two sets of figures may be helpful in determining suboptimal thrust logic to maintain the required orbit. The radial and cylindrical thrust vector components vary with the change in modulus k for the same value of circular orbit radius a. Because the only way to minimize the total amount of thrust is to minimize these components, care should be taken when determining a proper modulus k.

IX. Conclusions

A hypothetical elliptic integral solution to Jacobi's integral equation in the circular restricted three-body problem, under planar circular assumptions with nonuniform speed, has been offered. The solution, which satisfies one motion equation precisely and the other two approximately, provides closed-form analytical results for the orbital period and path in terms of several parameters including the orbit radius, the plane location, and the elliptic modulus (initial conditions). These suppositional results are found to be mathematically rich and insightful. However, to bridge the gap from hypothetical to factual, an iterative analytical approximate procedure that computes successive corrections to the hypothetical solution is also offered. An initial test case using a small L_1 periodic halo orbit showed, after a single correction step using simplifying assumptions, the corrections bring the hypothetical solution closer to the true orbit.

Results presented in the paper capture the essence of, and are dynamically relevant to, highly inclined orbits located near the collinear equilibrium points in the circular restricted three-body problem. The findings provide a window for deeper physical understanding of detail characteristics associated with this class of orbits. Results may provide practical utility for mission design and celestial analysis.

References

[1] Szebehely, V. G., *Theory of Orbits—The Restricted Problem of Three Bodies*, Academic Press, New York, 1967.

[2] Battin, R. H., *An Introduction to the Mathematics and Methods of Astrodynamics*, American Institute of Aeronautics and Astronautics, New York, 1987.

[3] Lagrange, J. L., "Essay on the Problem of Three Bodies," *Works of Lagrange*, edited by M. J.-A. Serret, Vol. 6, Gauthier-Villars, Paris, 1873, pp. 229–331.

[4] Jacobi, C. G. J., "On the Movement of a Point and on a Particular Case of the Problem of Three Bodies," *Reports of the Academy of Sciences of Paris*, Vol. 3, 1836, pp. 59–61.

[5] Hill, G. W., "Researches in the Lunar Theory," *American Journal of Mathematics*, Vol. 1, No. 1, 1878, pp. 5–26. doi:10.2307/2369430

[6] Moulton, F. R., *An Introduction to Celestial Mechanics*, Dover, New York, 1914.

[7] Lundberg, J., Szebehely, V., Nerem, R. S., and Beal, B., "Surfaces of Zero Velocity in the Restricted Problem of Three Bodies," *Celestial Mechanics*, Vol. 36, No. 2, June 1985, pp. 191–205. doi:10.1007/BF01230651

[8] Schaub, H., and Junkins, J. L., *Analytical Mechanics of Space Systems*, American Institute of Aeronautics and Astronautics, Reston, Virginia, 2005.

[9] MacMillan, W. D., "An Integrable Case in the Restricted Problem of Three Bodies," *The Astronomical Journal*, Vol. 27, No. 625–626, May 1911, pp. 11–13.

[10] Sitnikov, K., "The Existence of Oscillatory Motions in the Three-Body Problem," *Soviet Physics Doklady*, Vol. 5, No. 4, Jan. 1961, pp. 647–650.

[11] Moulton, F. R., *Periodic Orbits*, Carnegie Institute of Washington Publications, 161, Washington, D.C., 1920.

[12] Howell, K. C., "Families of Orbits in the Vicinity of the Collinear Libration Points," *Journal of the Astronautical Sciences*, Vol. 49, No. 1, Jan.–March, 2001, pp. 107–125.

[13] Farquhar, R. W., and Kamel, A. A., "Quasi-Periodic Orbits About the Translunar Libration Point," *Celestial Mechanics*, Vol. 7, No. 4, 1973, pp. 458–473. doi:10.1007/BF01227511

[14] Richardson, D. L., "Analytic Construction of Periodic Orbits About the Collinear Points," *Celestial Mechanics*, Vol. 22, No. 3, Oct. 1980, pp. 241–253. doi:10.1007/BF01229511

[15] Breakwell, J., and Brown, J., "The 'Halo' Family of 3-Dimensional Periodic Orbits in the Earth-Moon Restricted 3-Body Problem," *Celestial Mechanics*, Vol. 20, No. 4, 1979, pp. 389–404. doi:10.1007/BF01230405

[16] Henon, M., "Vertical Stability of Periodic Orbits in the Restricted Problem, I. Equal Masses," *Astronomy and Astrophysics*, Vol. 28, 1973, pp. 415–426.

[17] Zagouras, C. G., and Kazantzis, P. G., "Three-Dimensional Periodic Oscillations Generating from Plane Periodic Ones Around the Collinear Lagrangian Points," *Astrophysics and Space Science*, Vol. 61, No. 2, April 1979, pp. 389–409. doi:10.1007/BF00640540

[18] Robin, I. A., and Markellos, V. V., "Numerical Determination of Three-Dimensional Periodic Orbits Generated from Vertical Self-Resonant Satellite Orbits," *Celestial Mechanics*, Vol. 21, No. 4, 1980, pp. 395–434. doi:10.1007/BF01231276

[19] Ichtiaroglou, S. S., and Michalodimitrakis, M., "Three-Body Problem: The Existence of Families of Three-Dimensional Periodic Orbits Which Bifurcate from Planar Periodic Orbits," *Astronomy and Astrophysics*, Vol. 81, No. 1–2, 1980, pp. 30–32.

[20] Marchal, C., *The Three-Body Problem*, Elsevier, New York, 1990.

[21] Barden, B. T., and Howell, K. C., "Fundamental Motions Near Collinear Libration Points and Their Transitions," *Journal of the Astronautical Sciences*, Vol. 46, No. 4, Oct.–Dec. 1998, pp. 361–378.

[22] Gomez, G., Masdeont, J., and Simo, C., "Quasihalo Orbits Associated with Libration Points," *Journal of the Astronautical Sciences*, Vol. 46, No. 2, April–June, 1998, pp. 135–176.

[23] Valtonen, M., and Karttunen, H., *The Three-Body Problem*, Cambridge Univ. Press, Cambridge, England, U.K., 2006.

[24] Ghazy, M., and Newman, B., "Iterated Analytical Solution to the Restricted Problem of Three Bodies," AIAA/AAS Paper 2008-6430, 18–21 Aug. 2008.

[25] Armitage, J. V., and Eberline, W. F., *Elliptic Functions*, Cambridge Univ. Press, Cambridge, England, U.K., 2006.

[26] Abramowitz, M., and Stegun, I. A., *Handbook of Mathematical Functions with Formulas, Graphs, and Mathematical Tables*, Dover, New York, 1965.

[27] Howell, K. C., "Three-Dimensional, Periodic, 'Halo' Orbits," *Celestial Mechanics*, Vol. 32, No. 1, Jan. 1984, pp. 53–71. doi:10.1007/BF01358403